International Journal of Solids and Structures 196–197 (2020) 76–98

Contents lists available at ScienceDirect

International Journal of Solids and Structures

journal homepage: www.elsevier.com/locate/ijsolstr

Crack kinking in isotropic and orthotropic micropolar peridynamic solids

Vito Diana[a,*], Roberto Ballarini[b]

[a] Department ABC, Politecnico di Milano, Piazza Leonardo da Vinci 32, Milano, 20133, Italy
[b] Department of Civil & Environmental Engineering, University of Houston, 4726 Calhoun Road, Houston, TX, 77204-4003, USA

ARTICLE INFO

Article history:
Received 18 November 2019
Revised 26 March 2020
Accepted 30 March 2020
Available online 3 April 2020

Keywords:
Peridynamics
Orthotropy
Micropolar
Fracture criteria
Crack kinking

ABSTRACT

A micropolar peridynamic model is presented for characterizing crack propagation in isotropic and orthotropic brittle materials. The analytical formulation of the two-dimensional model is based on the definition of a micropotential energy function that accounts for the four independent elastic constants that define orthotropy and that in the limit can be reduced to isotropy. A distinctive feature of the model is that the bonds' elastic parameters are continuous functions of orientation with respect to principal material axes. By defining three deformation parameters that quantify bond stretch, bond shear deformation and particles relative rotation, the first continuum bond-based peridynamic model is obtained for two-dimensional Cauchy orthotropic materials characterized by four independent material moduli that is suitable for describing fracture as well as homogeneous and non-homogeneous deformations.

The accuracy of the computational model as applied to crack-tip analyses is assessed by comparing the displacement and stress fields within the boundary layer that develops in the immediate vicinity of a crack with the analytical asymptotic results for an orthotropic continuum. The extension of such cracks when they are subjected to mixed-mode loading is simulated under the assumption of illustrative crack extension criteria, and the predictions are compared to those of the maximum hoop stress intensity factor criterion (HSIF-criterion) and the maximum energy release rate criterion (G-criterion).

1. Introduction

Peridynamic (PD) theory (Silling, 2000) represents the mechanical behavior of solids not through differential equations as in the case of classical continuum mechanics, but instead with integro-differential equations that do not involve spatial derivatives. This aspect lends itself to the description of discontinuities such as cracks. Numerous PD formulations have been published; the larger (smaller) portion involves isotropic (anisotropic) materials. A brief review of PD for elasticity and fracture mechanics is warranted. With respect to isotropy, significant efforts were aimed at reproducing linear elastic behavior, and in particular to resolve the problem of fixed Poisson's ratio associated with the original formulation. In fact, the originally proposed PD, referred to as bond-based PD (BBPD), is a central force model. Therefore, as in the rari-constant theory (Navier, 1827; Cauchy, 1850; Truesdell, 1984), Poisson's ratio is restricted to $\nu = 1/4$ for three-dimensional (3D) and plane strain configurations, and $\nu = 1/3$ for plane stress. To overcome this limitation, Silling et al. (2007) developed the state-based PD formulation (SBPD) in which the force between two particles depends on the deformations of all particles within their neighborhood. Other efforts along these lines include the non-ordinary state-based model (NOSB), a tool for adapting classical material models for use with PD and for simulating a material with other types of constitutive models (Warren et al., 2009).

However, in the context of bond-based models, Wang et al. (2018, 2017) derived a conjugated bond-pair-based PD formulation inspired by the Keating model (Keating, 1966) and characterized by two independent elastic constants. Liu and Hong (2012) proposed an approach based on a force compensation scheme and Zhu and Ni (2017) derived a PD formulation that accounts for single bond shear deformation and thus produces different values of Poisson's ratio. Gerstle introduced a two-parameter micropolar isotropic PD model (Gerstle et al., 2007) comprised of an Euler-Bernoulli beam-like microstructure. Recently, Diana and Casolo (2019a) proposed a generalized micropolar peridynamic formulation with three bond stiffness moduli and inspired by Voigt's studies on crystals (Voigt, 1887). PD theory has been ap-

* Corresponding author.
E-mail address: vito.diana@polimi.it (V. Diana).

https://doi.org/10.1016/j.ijsolstr.2020.03.025
0020-7683/

plied extensively to problems involving fracture (Bobaru et al., 2012; Madenci and Oterkus, 2014; Casolo and Diana, 2018; Shojaei et al., 2018; Roy et al., 2017), plasticity and viscoelasticy (Madenci and Oterkus, 2016; Rahaman et al., 2017; Weckner and Mohamed, 2013), thermo-mechanical effects (Oterkus et al., 2014) and corrosion (Chen and Bobaru, 2015). Unlike other computational paradigms such as the finite element method and the boundary element method in which the nucleation and extension of cracks requires cumbersome remeshing procedures, in PD cracking is a consequence of the movement of material points. This feature makes PD very attractive for the simulation of failure and in particular the interaction between relatively large numbers of cracks.

Anisotropic PD models have been proposed by Hu et al. (2011), Oterkus and Madenci (2012), Xu et al. (2008), and Colavito et al. (2007), to simulate crack propagation in composites with uni-directional fibers. The aforementioned models are based on a homogenization approach in which the stiffness of the PD bonds parallel to the fiber direction (fiber bonds) is fitted to the elastic modulus of the lamina in the same direction, and all other bonds (matrix bonds) have their stiffness fitted to the lamina properties along the direction perpendicular to the fiber orientation. In Hu and Madenci (2016) and Diyaroglu et al. (2019), the ligaments are distinguished in normal and shear bonds depending on their spatial orientations. Kilic et al. (2009) developed a microscale PD model with fiber and matrix phases represented as distinct material points, and used it to predict matrix damage in laminated composites, accounting for the inhomogeneous distinct properties of the fiber and matrix. These models have been able to provide predictions of fiber/matrix fracture and delamination that are in good qualitative agreement with experimental observations. The model presented by Hu et al. (2012) for unidirectional fiber-reinforced composites can be used for any grid orientation relative to the fiber direction, but it suffers from fixed values of Poisson's ratio and shear modulus. Askari et al. (2008) proposed another PD model in their study of crack propagation in a poly-crystalline microstructure. Ghajari et al. (2014) proposed the first continuous PD model for orthotropic media based on the use of eighth-order sinusoidal functions. Similar PD formulations for orthotropic material were also proposed later by le Hu et al. (2014) and by Zhou et al. (2017). However, since such orthotropic models are based on a classical bond-based PD formulation, only two elastic moduli can be independently prescribed. A discrete full orthotropic bond-based PD model has been proposed recently by Diyaroglu et al. (2019). In the context of SBPD instead, an orthotropic PD model for linearly elastic solids was proposed by Mikata (2018). It can be seen that in SBPD or classical BBPD there are no forces out of the bond direction representing the shear force due to shear deformation (Rabczuk and Ren, 2017; Ren et al., 2016). Moreover, state-based PD models may be associated with a larger computational cost with respect to bond-based models (Zhang et al., 2018).

In this paper, the micropolar peridynamic (MPPD) formulation recently presented (Diana and Casolo, 2019a; 2019b), is extended to fracture and is applied to the study of crack initiation, kinking and propagation in isotropic and orthotropic brittle materials. It is based on the use of continuous trigonometric functions and differs from other bond-based orthotropic peridynamic models which are limited to two independent material constants. The conceived model is based on the definition of three deformation parameters: the bond stretch; the bond shear deformation that accounts for the rotational degrees of freedom; and the particle's relative rotation. The formulation results, for the first time, in a continuous bond-based PD model for 2D Cauchy orthotropic materials characterized by four independent material moduli that is suitable for describing fracture as well as homogeneous and non-homogeneous deformations. Since three different stiffness parameters for each peridynamic ligament can be independently defined and calibrated, the model can be also be potentially extended to Cosserat orthotropic materials (Diana and Casolo, 2019a).

This paper is structured as follows. In Section 2, an analytical implicit linearized formulation of the proposed micropolar peridynamic model is given. Particular attention is paid to its numerical implementation. The generalized three-parameter micropolar model is derived by defining specific deformation measures related to axial, shear and particles' relative rotation deformations. In this way, the PD micropotential energy function is written, and the generalized MPPD bond stiffness operator is obtained. The analytical expression of the four independent peridynamic constants for orthotropic materials are thus given. The two-parameter isotropic micropolar PD model is then obtained as a special case, by specifying that the shear and axial stiffnesses are independent of the bond angle of inclination. Moreover an energetic failure criterion is presented in this section. Section 3 assesses the accuracy of the PD description of the stress and deformations that develop in the immediate vicinity of a crack-tip subjected to mixed-mode loading, and the directions the crack will kink/curve. Illustrative examples involve a boundary layer analysis in which the boundaries of the computational model are subjected to the well-known asymptotic results for elastic isotropic and orthotropic materials. First, the numerical results calculated for the stationary crack are compared with these asymptotic formulas. Second, the directions of crack kinking/curving simulated using two illustrative extension criteria are compared to those associated with the maximum hoop stress intensity factor criterion (HSIF-criterion) and the maximum energy release rate fracture criterion (G-criterion). In the case of isotropic materials, the influence of the Poisson's ratio on the crack kinking angles is also investigated.

It is noted that all results are generated using MATLAB (Matlab, 2017) computing within a UNIX environment. The post-processing of the results is instead performed using PARAVIEW, MATLAB and OVITO (Stukowski, 2009).

2. The micropolar peridynamic model

In micropolar Peridynamics (MPPD) the particles' translational degrees of freedom are augmented, in two dimensions, to include a rotational degree of freedom θ (Gerstle et al., 2009). In this way, the equations of motion for any infinitesimal material particle at $\mathbf{X}$ in the reference configuration at time t are derived from

$$\rho\ddot{\mathbf{u}}(\mathbf{X},t) - \int_{H_{\mathbf{X}}} \mathbf{f}(\mathbf{u}' - \mathbf{u}, \mathbf{X}' - \mathbf{X}) dV_{\mathbf{X}'} - \mathbf{b}(\mathbf{X},t) = \mathbf{0} \quad \text{for} \quad \mathbf{X} \in \Omega, \tag{1}$$

$$\mathbf{J}\ddot{\boldsymbol{\theta}}(\mathbf{X},t) - \int_{H_{\mathbf{X}}} \mathbf{m}(\mathbf{u}' - \mathbf{u}, \mathbf{X}' - \mathbf{X}) dV_{\mathbf{X}'} - \mathbf{c}(\mathbf{X},t) = \mathbf{0} \quad \text{for} \quad \mathbf{X} \in \Omega, \tag{2}$$

where Ω is the domain occupied by the body, whereas $\mathbf{X}' - \mathbf{X} = \boldsymbol{\xi}$ and $\mathbf{u}' - \mathbf{u} = \boldsymbol{\eta}$ are the relative position and the relative displacement between the material points $\mathbf{X}$ and $\mathbf{X}'$ (see Fig. 1). The body force vector is $\mathbf{b}$, and $\mathbf{f}$ is the pairwise force. The applied body couple is indicated by $\mathbf{c}$, $\ddot{\boldsymbol{\theta}}$ is the angular acceleration vector, and $\mathbf{J}$ denotes the mass moment of inertia per unit volume tensor. The integrals are defined over a region $H_{\mathbf{X}}$ referred to as the family of $\mathbf{X}$ (i.e. the horizon region of radius δ). The linear and angular momentum equilibrium equations at time t in discretized form of are:

$$\sum_{j=1} \mathbf{f}(\mathbf{u}_j - \mathbf{u}_i, \mathbf{X}_j - \mathbf{X}_i)\Delta V_j + \mathbf{b}_i = \rho\ddot{\mathbf{u}}_{\mathbf{i}} \tag{3}$$

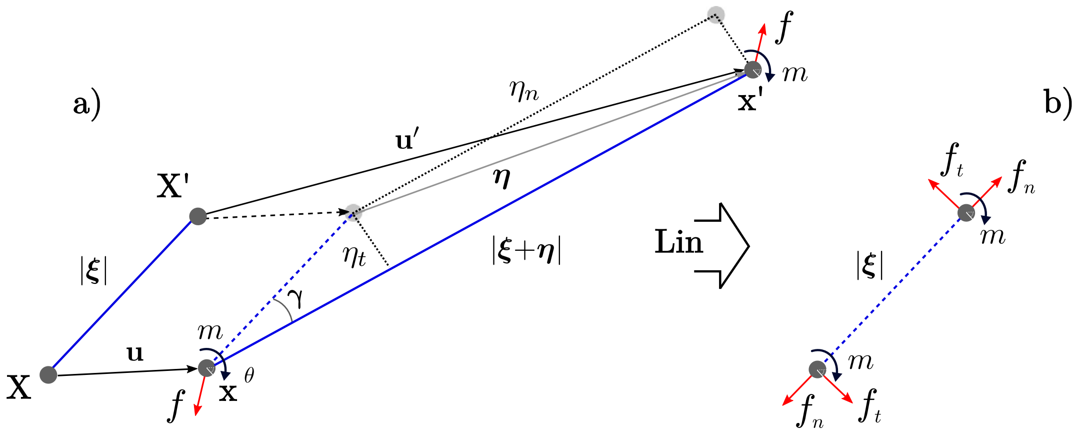

Fig. 1. (a) Undeformed and deformed configuration of a micropolar peridynamic bond; (b) Linearized theory.

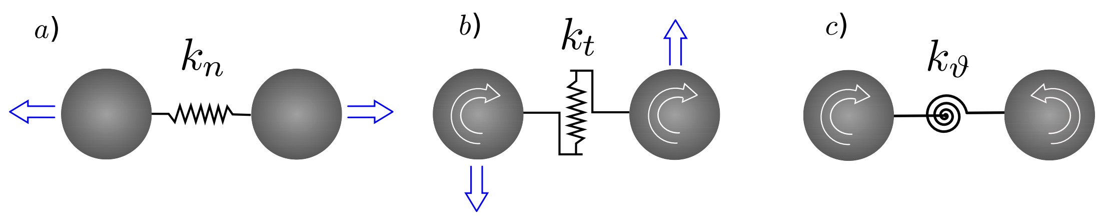

Fig. 2. Sketch of the interactions between two particles: (a) due to normal spring, (b) due to shearing spring, (c) due to rotational spring.

$$\sum_{j=1} \mathbf{m}(\mathbf{u}_j - \mathbf{u}_i, \mathbf{X}_j - \mathbf{X}_i)\Delta V_j + \mathbf{c}_i = \mathbf{J}\ddot{\boldsymbol{\theta}}_i \tag{4}$$

where subscript j denotes a particle within the horizon region of particle i. Thus the sum in Eq. (3) is taken over all nodes j such that $|\mathbf{X}_j - \mathbf{X}_i| \le \delta$ (i.e. neighboring particles of particle i). By using mesh generation tools developed for finite-element analyses, the structure is discretized into a set of subvolumes, each of which contains at its centroid a single PD material point. Subsequently a Γ algorithm determines the neighboring particles of each particle of the discretization. A quadrature scheme in which partial neighbor intersections are also considered has been implemented. The results of the partial neighbor intersection computation, and thus the value of the volume correction coefficient α is calculated by Liu and Hong (2012)

$$\alpha(|\boldsymbol{\xi}|) = \begin{cases} \frac{\xi-\delta+0.5\Delta x}{\Delta x} & \text{if} \quad (\delta - 0.5\Delta x) < |\boldsymbol{\xi}| \le \delta \\ 1 & \text{if} \quad |\boldsymbol{\xi}| \le (\delta - 0.5\Delta x) \\ 0 & \quad \text{otherwise} \end{cases} \tag{5}$$

where Δx is the grid spacing.

In MPPD each bond connecting two particles i and j can be idealized as an assemblage of two translational springs and a rotational spring (Diana and Casolo, 2019a) (Fig. 2). The force and displacements vectors in a local coordinate system are

$$\{f\}^T = \{f_n^i \quad f_t^i \quad m^i \quad f_n^j \quad f_t^j \quad m^j\} \tag{6}$$

$$\{u\}^T = \{u_n^i \quad u_t^i \quad \theta^i \quad u_n^j \quad u_t^j \quad \theta^j\} \tag{7}$$

Therefore three bond deformation parameters can be defined that are functions of the relative displacements in the normal, tangential, and rotational sense, respectively (see Fig. 2 and 3). The deformation in the normal direction is the classical peridynamic bond stretch s,

$$s = \frac{|\boldsymbol{\xi} + \boldsymbol{\eta}| - |\boldsymbol{\xi}|}{|\boldsymbol{\xi}|} \tag{8}$$

which in a linearized theory is written as

$$s = \frac{1}{|\boldsymbol{\xi}|}\left(\boldsymbol{\eta} \cdot \frac{\boldsymbol{\xi}}{|\boldsymbol{\xi}|}\right) = \frac{\eta_n}{|\boldsymbol{\xi}|} = \frac{(u_n^j - u_n^i)}{|\boldsymbol{\xi}|} \tag{9}$$

where η_n is the component of $\boldsymbol{\eta}$ along the undeformed bond of unit vector $\boldsymbol{\xi}/|\boldsymbol{\xi}|$. The shearing deformation is

$$\gamma = \frac{\eta_t}{|\boldsymbol{\xi}|} - \bar{\theta} = \frac{(u_t^j - u_t^i)}{|\boldsymbol{\xi}|} - \frac{(\theta^j + \theta^i)}{2} \tag{10}$$

defined as the difference between the rotation angle of the ligament and the particles' average rotation. The latter reduces or increases the bond shear deformation depending on the mutual rotation sense of the particles itself. In particular, if the two particles rotate with an equal and opposite angle θ, the rotation contribution to the bond shear deformation is null. The deformation parameter associated with the rotational bond spring is defined by the relative particles' rotation measure, i.e. the difference between the rotation angles of the two connected particles[1]

$$\vartheta = (\theta^j - \theta^i) \tag{12}$$

The compatibility equation can be written in a compact form as

$$\{h\} = [B]^T\{u\} \tag{13}$$

where $\{h\} = \{s \quad \gamma \quad \vartheta\}^T$ is the vector of the springs deformation measures and $[B]^T$ is defined by

$$[B]^T = \frac{1}{|\boldsymbol{\xi}|}\begin{bmatrix} -1 & 0 & 0 & 1 & 0 & 0 \\ 0 & -1 & -|\boldsymbol{\xi}|/2 & 0 & 1 & -|\boldsymbol{\xi}|/2 \\ 0 & 0 & -|\boldsymbol{\xi}| & 0 & 0 & |\boldsymbol{\xi}| \end{bmatrix} \tag{14}$$

[1] This parameter can be used to improve the bond stretch measure in such a way that $s = \frac{(u_n^j - u_n^i) + \kappa\vartheta}{|\boldsymbol{\xi}|}$ (11) where κ is a scaling parameter which regulates how much bending is considered in the bond stretch measure (for simplicity it is usually set to zero) (Karihaloo et al., 2003; Pan et al., 2018; Lilliu and van Mier, 2003).

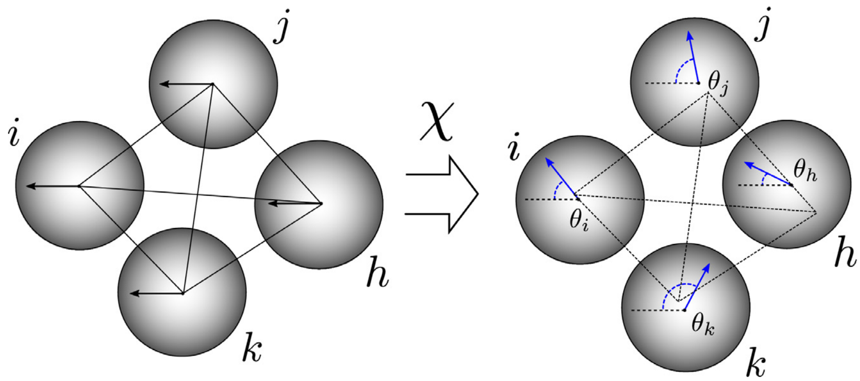

Fig. 3. Schematics of typical particles initial and deformed configuration for bond-based micropolar peridynamics. The particles orientation changes as result of the deformation process.

The constitutive behavior of the model is defined by the following relation

$$\{q\} = [D]\{h\} \longrightarrow \begin{Bmatrix} f_n \\ f_t \\ m_\vartheta \end{Bmatrix} = \begin{bmatrix} k_n & 0 & 0 \\ 0 & k_t & 0 \\ 0 & 0 & k_\vartheta \end{bmatrix} \begin{Bmatrix} s \\ \gamma \\ \vartheta \end{Bmatrix} \tag{15}$$

where $[D]$ is a diagonal matrix[2] containing the bond normal, tangential, and rotational stiffnesses, and relates the peridynamic actions between two particles to the parameters of bond deformation defined above. The pairwise bond couple and forces can be viewed as the springs' reactions to the bond deformations s and γ and ϑ, respectively. Note that m_ϑ represents the self-equilibrated part of the particles microcouples in a specific ligament.

It is worth noting that the conceived general MPPD formulation can lead to different centrosymmetric models depending on the specific constitutive parameters k_n, k_t and k_ϑ adopted. An important consideration is that the shear stiffness parameter k_t has the same dimensions of the normal stiffness parameter k_n and is conceptually related to the shear modulus G of classical elasticity (Diana and Casolo, 2019b).

The general form of the macroelastic energy density $\Phi(\mathbf{X})$ for micropolar peridynamics is obtained by considering the contribution of the three springs and their corresponding deformation measures such that

$$\Phi(\mathbf{X}) = \frac{1}{2}\int_{H_\mathbf{X}} (\mathrm{w}_s + \mathrm{w}_\gamma + \mathrm{w}_\vartheta)\, dV_{\mathbf{X}'} = \frac{1}{2}\int_{H_\mathbf{X}} \frac{k_n s^2|\boldsymbol{\xi}|}{2} + \frac{k_t\gamma^2|\boldsymbol{\xi}|}{2} + \frac{k_\vartheta\vartheta^2}{2} dV_{\mathbf{X}'} \tag{16}$$

with $\mathrm{w} = (\mathrm{w}_s + \mathrm{w}_\gamma + \mathrm{w}_\vartheta)$ defined as the micropotential energy function satisfying the conditions of microelasticity (Silling, 2000)

$$f_n = \frac{\partial \mathrm{w}_s}{\partial \eta_n}; \qquad f_t = \frac{\partial \mathrm{w}_\gamma}{\partial \eta_t}; \qquad m_\vartheta = \frac{\partial \mathrm{w}_\vartheta}{\partial \vartheta} \tag{17}$$

The macroelastic potential energy of a micropolar peridynamic body is then given by

$$\hat{\Phi} = \frac{1}{2}\int_\Omega\int_{H_\mathbf{X}} \frac{k_n s^2|\boldsymbol{\xi}|}{2} + \frac{k_t\gamma^2|\boldsymbol{\xi}|}{2} + \frac{k_\vartheta\vartheta^2}{2} dV_{\mathbf{X}'}dV_\mathbf{X} \tag{18}$$

For a single bond of length $|\boldsymbol{\xi}|$ between two particles i and j, we can write a discrete form of the balance of the variation of the total macroelastic energy and the work W done by the external nodal forces $\{p\}$ as

$$\hat{\Phi} = \frac{1}{2}\{u\}^T\frac{1}{2}[B][D][\xi]\Delta V_i\alpha\Delta V_j[B]^T\{u\} = \frac{1}{2}\{u\}^T\{p\} = W \tag{19}$$

[2] When considering non-isotropic materials, the $[D]$ matrix which describes the constitutive behavior of the bond is function of the orientation (ψ) angle of the ligament, since at each angle correspond a specific set of stiffnesses.

where, due to Eq. (16)

$$[\xi] = \begin{bmatrix} |\boldsymbol{\xi}| & 0 & 0 \\ 0 & |\boldsymbol{\xi}| & 0 \\ 0 & 0 & 1 \end{bmatrix} \tag{20}$$

The bond stiffness matrix in the global coordinate system can be expressed by

$$[K]_{bond} = \alpha\Delta V_i\Delta V_j[R]^T[B][D][\xi][B]^T[R] \tag{21}$$

where $[R]$ is a rotation matrix. It is interesting to note that the micropolar peridynamic model with frame-like ligaments connecting particles, i.e. a 2D non-local lattice with Euler-Bernoulli beam-like microstructure (e.g. Gerstle's isotropic micropolar model (Gerstle et al., 2009)), is a special case of the conceived model described in this section. Further details regarding this aspect can be found in Diana (2019); Diana and Casolo (2019b).

2.1. The definition of the peridynamic traction vector

Towards the goal of studying not only deformation in the vicinity of a crack tip, at this point it is interesting to introduce a specific stress measure for micropolar peridynamics which is strictly related to the original stress definition by Saint Venant (1845) and accepted later by Timoshenko (1983) and Lehoucq and Silling (2008). For more details regarding the concept of stress in PD, see Ballarini et al. (2018).

Considering an arbitrary plane π passing through $\mathbf{X}$ which has a normal vector $\mathbf{n}^*$ and divides the family region $H_\mathbf{X}$ into two pieces, the force which one part exerts on the other can be expressed as

$$\mathbf{F}(H_{\mathbf{X}^+}, H_{\mathbf{X}^-}) = \int_{H_\mathbf{X}^-}\int_{H_\mathbf{X}^+} \mathbf{f}(\mathbf{u}'' - \mathbf{u}', \mathbf{X}'' - \mathbf{X}')dV_{\mathbf{X}''}V_{\mathbf{X}'} \tag{22}$$

The line segment $\mathbf{X}'' - \mathbf{X}'$ given by two interacting material points intersects the dividing plane π at a unique point $\mathbf{X}$. The line segment $\mathbf{X}'' - \mathbf{X}$ has the length ζ and points in the outer direction $\mathbf{v}$, i.e. $\mathbf{v}\cdot\mathbf{n}^* > 0$. The line segment $\mathbf{X} - \mathbf{X}'$ has the length υ and points in the opposite direction such that

$$\mathbf{X}'' = \mathbf{X} + \zeta\mathbf{v}; \qquad \mathbf{X}' = \mathbf{X} - \upsilon\mathbf{v} \tag{23}$$

The integration over all interacting couples $[\mathbf{X}''; \mathbf{X}']$ can be rewritten as a surface integral over the contact plane π of a corresponding surface density, i.e. the traction vector $\mathbf{t}(\mathbf{X}, \mathbf{n}^*)$. Hence, the PD traction vector with respect to plane π, with outward pointing unit normal $\mathbf{n}^*$ at point $\mathbf{X}$ is now defined by Lehoucq and Silling (2008)

$$\mathbf{t}(\mathbf{X}, \mathbf{n}^*) = \frac{1}{2}\int_\mathcal{L}\int_0^\delta\int_0^\delta (\zeta+\upsilon)^2\mathbf{f}[\mathbf{u}'' - \mathbf{u}', \mathbf{v}(\zeta+\upsilon)]\mathbf{v}\cdot\mathbf{n}^* d\zeta\, d\upsilon\, d\omega_\mathbf{v} \tag{24}$$

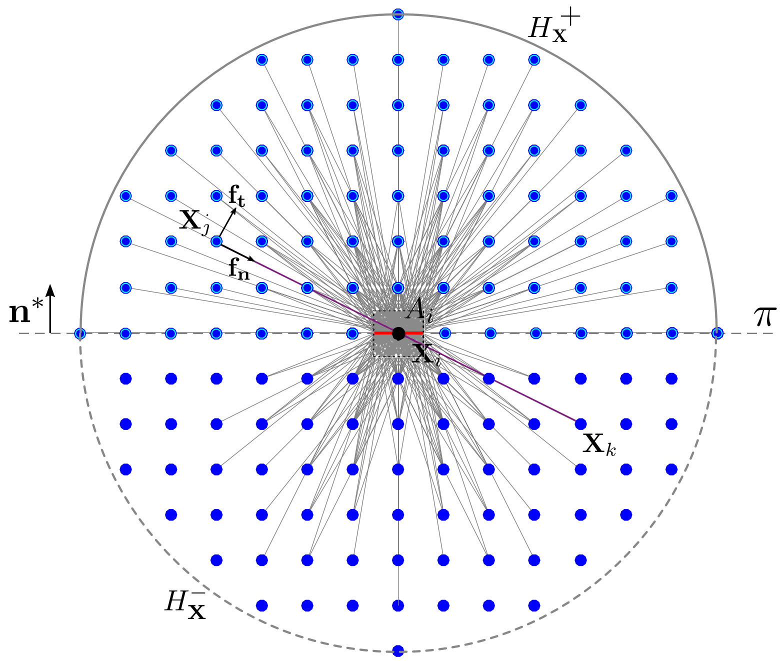

Fig. 4. Definition of the micropolar PD traction vector at point $\mathbf{X_i}$ according to Eq. (25) with respect to plane π of outward pointing unit normal $\mathbf{n^*}$. The pairwise force $\mathbf{f}$ is characterized by normal and tangential components $\mathbf{f_n}$ and $\mathbf{f_t}$.

where $\mathcal{L}$ denotes the unit sphere, and $d\omega_\mathbf{v}$ denotes a differential solid angle on $\mathcal{L}$ in the direction of any unit vector $\mathbf{v}$. The factor of 1/2 appears in Eq. (24) because the integral sums the forces on $\mathbf{X'}$ due to $\mathbf{X''}$ and those on $\mathbf{X''}$ due to $\mathbf{X'}$ (Silling and Lehoucq, 2008; Lehoucq and Silling, 2008). Eq. (24) can be simplified and written in discrete form as

$$\begin{aligned}\mathbf{t}(\mathbf{X}_i,\mathbf{n}^*) &= \frac{1}{A_i}\sum_{k=1}^{H^-}\sum_{j=1}^{H+}\mathbf{f}(\mathbf{u}_j-\mathbf{u}_k,\mathbf{X}_j-\mathbf{X}_k)\Delta V_j\Delta V_k \\ &= \frac{1}{A_i}\sum_{k=1}^{H^-}\sum_{j=1}^{H+}\Big[f_n(\mathbf{u}_j-\mathbf{u}_k,\mathbf{X}_j-\mathbf{X}_k)\frac{\boldsymbol{\eta_n}}{|\boldsymbol{\eta_n}|} \\ &\quad + f_t(\mathbf{u}_j-\mathbf{u}_k,\mathbf{X}_j-\mathbf{X}_k)\frac{\boldsymbol{\eta_t}}{|\boldsymbol{\eta_t}|}\Big]\Delta V_j\Delta V_k \end{aligned} \tag{25}$$

where H^- is the number of particles in the negative side of the i-particle's horizon. The summation involves only the set of bonds passing through or ending at the cross section A_i from the positive side, as Fig. 4 shows. Obviously, following Eq. (24) the same operation involving this time the bonds from the negative side is also required. The sought traction vector is then given by the average of these two values.

This being a micropolar model, the pairwise force $\mathbf{f}$ is characterized by normal and tangential components $\mathbf{f_n}$ and $\mathbf{f_t}$. The normal and tangential components of the traction vector defined above are the normal and shear stress

$$\sigma_{n^*n^*} = \mathbf{t}(\mathbf{X}_i,\mathbf{n}^*)\cdot\mathbf{n}^* \tag{26}$$

$$\tau_{n^*v} = \mathbf{t}(\mathbf{X}_i,\mathbf{n}^*)\cdot\mathbf{v} \tag{27}$$

where $\mathbf{v}$ denotes the direction orthogonal to that of the outer normal $\mathbf{n^*}$.

2.2. A full orthotropic micropolar peridynamic formulation

The classical elasticity stress-strain relations (Hooke's law) for an orthotropic material under plane-stress or plane-strain conditions in the principal material directions, inclined at angle ζ with respect to the horizontal, can be written using the Voigt notation as:

$$\{\sigma\} = [\mathbf{C}]\{\epsilon\} \longrightarrow \begin{Bmatrix}\sigma_1\\ \sigma_2\\ \tau_{12}\end{Bmatrix} = \begin{bmatrix}C_{11} & C_{12} & 0\\ C_{12} & C_{22} & 0\\ 0 & 0 & C_{66}\end{bmatrix}\begin{Bmatrix}\epsilon_1\\ \epsilon_2\\ \gamma_{12}^*\end{Bmatrix} \tag{28}$$

Assuming for simplicity that $\zeta = 0$, and thus considering a generic coordinate system xy rotated by ψ with respect to the horizontal, Eq. (28) can be rewritten as

$$\{\sigma\}^\psi = [\mathbf{C}]^\psi\{\epsilon\}^\psi \tag{29}$$

being $[\mathbf{C}]^\psi$ defined as

$$\begin{aligned}[\mathbf{C}]^\psi &= \begin{bmatrix}C_{xx} & C_{xy} & C_{xs}\\ C_{xy} & C_{yy} & C_{ys}\\ C_{xs} & C_{ys} & C_{ss}\end{bmatrix} = [\mathbf{Q}]^{-1}[\mathbf{C}][\mathbf{Q}]^{-T} \\ &= [\mathbf{Q}]^{-1}\begin{bmatrix}C_{11} & C_{12} & 0\\ C_{12} & C_{22} & 0\\ 0 & 0 & C_{66}\end{bmatrix}[\mathbf{Q}]^{-T}\end{aligned} \tag{30}$$

where $[\mathbf{Q}]$ is

$$[\mathbf{Q}] = \begin{bmatrix}\cos^2\psi & \sin^2\psi & 2\cos\psi\sin\psi\\ \sin^2\psi & \cos^2\psi & -2\cos\psi\sin\psi\\ -\cos\psi\sin\psi & \cos\psi\sin\psi & \cos 2\psi\end{bmatrix} \tag{31}$$

Thus, the off-axis axial C_{xx} and shear C_{ss} moduli can be written as function of the direction defined by ψ, in terms of the four material constants defined in Eq. (28) as

$$\begin{aligned}C_{xx}(\psi) &= C_{11}\cos^4\psi + C_{22}\sin^4\psi + 2C_{12}\sin^2\psi\cos^2\psi \\ &\quad + 4C_{66}\sin^2\psi\cos^2\psi\end{aligned} \tag{32}$$

$$\begin{aligned}C_{ss}(\psi) &= C_{11}\sin^2\psi\cos^2\psi + C_{22}\sin^2\psi\cos^2\psi \\ &\quad -2C_{12}\sin^2\psi\cos^2\psi + C_{66}(\cos^2\psi - \sin^2\psi)^2\end{aligned} \tag{33}$$

By analogy with the continuum, assume for instance that in an orthotropic peridynamic solid, the axial and shear bond stiffness (i.e.

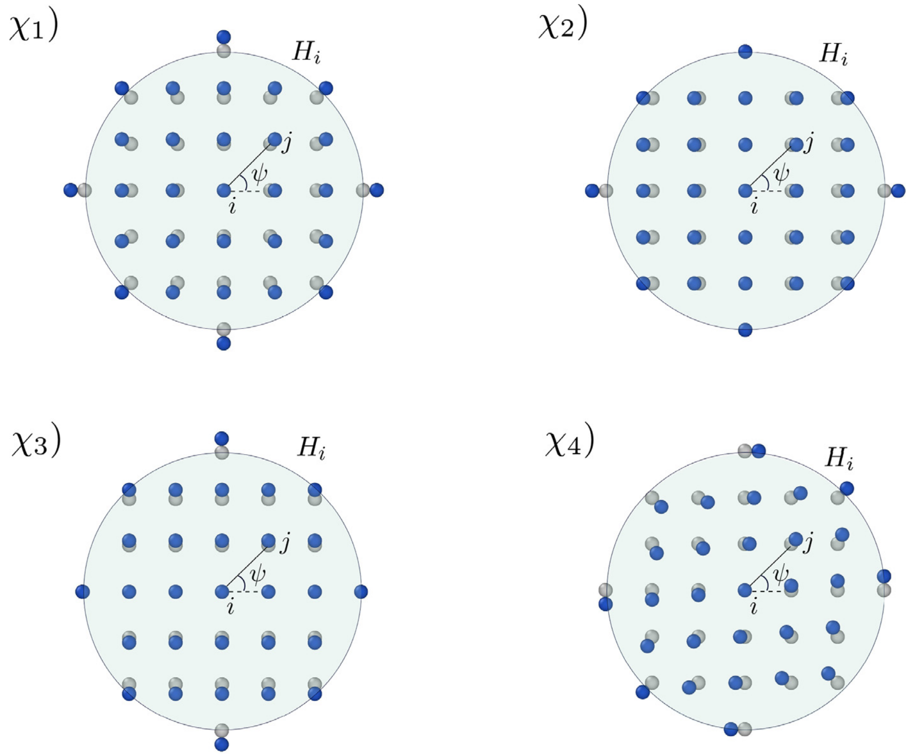

Fig. 5. Unit cells H_i subjected to: χ_1) isotropic expansion field of orthogonal PD stretch components $s_1 = s_2 = s$, $\gamma = 0$; χ_2) simple extension field of orthogonal PD stretch components $s_1 = s$, $s_2 = \gamma = 0$; χ_3) simple extension field of orthogonal PD stretch components $s_2 = s$, $s_1 = \gamma = 0$; χ_4) pure shear field of orthogonal PD stretch components $s_1 = s_2 = 0$, $\gamma = s$.

k_n and k_t) follow a law of variation with respect to ψ similar to that of C_{xx} and C_{ss} described by Eqs. (32) and (33), respectively, in such a way that

$$k_n(\psi) = k_{n_1}\cos^4\psi + k_{n_2}\sin^4\psi + 2k_v\sin^2\psi\cos^2\psi + 4k_{t_1}\sin^2\psi\cos^2\psi \tag{34}$$

$$k_t(\psi) = k_{n_1}\sin^2\psi\cos^2\psi + k_{n_2}\sin^2\psi\cos^2\psi - 2k_v\sin^2\psi\cos^2\psi + k_{t_1}(\cos^2\psi - \sin^2\psi)^2 \tag{35}$$

where k_{n_1} and k_{n_2} are the PD axial micromoduli along principal material axes, k_{t_1} is the shear micromodulus along one of the principal material axis[3] and k_v is a parameter related to the ratio between $k_t(\psi)$ and $k_n(\psi)$ in each direction. Hence, four independent PD micromoduli for describing the mechanical behavior of a 2D orthotropic solid have been defined.

The relation between the orthotropic peridynamic moduli, k_{n_1}, k_{n_2}, k_v and k_{t_1} and the classical continuum elastic constants in Eq. (28), is obtained following the approach introduced by Gerstle (2016). Given a specific homogeneous strain state, the macroelastic energy density in a specific point was determined from the PD formulation and it was set equal to the strain energy density determined from the classical theory of elasticity. Note that for homogeneous deformation states, the particles microrotations θ are null (Diana and Casolo, 2019a). To obtain the bond stretch and the bond shear deformation along a specific bond direction, the strain vector

$$\{\chi\} = \{s_1 \quad s_2 \quad \gamma\}^T \tag{36}$$

that defines a specific deformation state of $H_{\mathbf{X}}$, is transformed into a coordinate system whose first axis is aligned with the bond and the second axis is orthogonal to the bond. In this way, being ψ the angle of inclination of a specific bond with respect to the horizontal direction we obtain

$$s(\psi) = \frac{1}{2}[s_1 + s_2 + (s_1 - s_2)\cos 2\psi + 2\gamma\sin 2\psi] \tag{37}$$

$$\gamma(\psi) = \frac{1}{2}[(s_1 - s_2)\sin 2\psi - 2\gamma\cos 2\psi] \tag{38}$$

It is worth noting that when a PD unit cell (the neighborhood of $\mathbf{X}$ or the family of $\mathbf{X}$) is subjected to a specific homogeneous deformation state defined by Eq. (36), s_1 and s_2 are equivalent to ϵ_1 and ϵ_2 of the continuum. However γ in our model is a deformation measure referred to a single bond, thus in a pure shear deformation state, $\gamma = \gamma^*/2$, where γ^* is the shear deformation of the continuum. The four homogeneous deformation states considered in Fig. 5, can be described by the following deformation tensors:

$$[\mathbf{F}]_1 = \begin{bmatrix} 1+s & 0 \\ 0 & 1+s \end{bmatrix}; \quad [\mathbf{F}]_2 = \begin{bmatrix} 1+s & 0 \\ 0 & 1 \end{bmatrix};$$
$$[\mathbf{F}]_3 = \begin{bmatrix} 1 & 0 \\ 0 & 1+s \end{bmatrix}; \quad [\mathbf{F}]_4 = \begin{bmatrix} 1 & \gamma \\ \gamma & 1 \end{bmatrix} \tag{39}$$

which lead to the strain vectors

$$\{\chi\}_1 = \{s \quad s \quad 0\}^T \tag{40}$$

$$\{\chi\}_2 = \{s \quad 0 \quad 0\}^T \tag{41}$$

$$\{\chi\}_3 = \{0 \quad s \quad 0\}^T \tag{42}$$

[3] In Cauchy orthotropic materials in fact, $G_{11} = G_{22} = G$, hence $k_{t_1} = k_{t_2}$ (Ostoja-Starzewski, 2002; Diana and Casolo, 2019b).

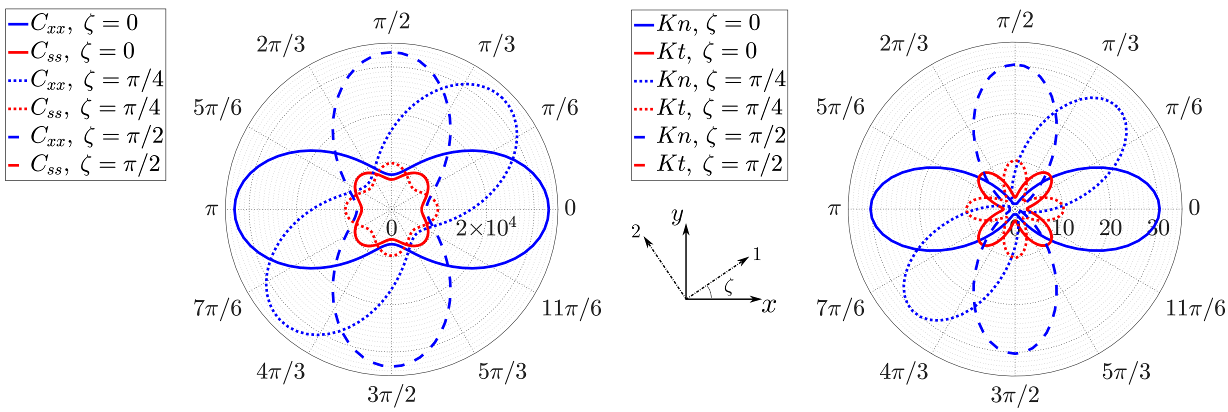

Fig. 6. Comparison of the off-axis C_{xx} and C_{ss} classical continuum moduli (in MPa) and k_n and k_t MPPD moduli (in N/mm^6) for an orthotropic material ($C_{11} = 33000$MPa; $C_{12} = 730$MPa; $C_{22} = 7300$MPa; $C_{66} = 6300$MPa in the cases of $\zeta = 0$; $\zeta = \pi/4$ and $\zeta = \pi/2$).

$$\{\chi\}_4 = \{0 \quad 0 \quad 2\gamma\}^T \tag{43}$$

where $s < \; < 1$ and $\gamma = s$. At this point we can derive the analytical expressions of the four classical continuum strain energy densities and the corresponding micropolar peridynamic macroelastic energy density functions, as described in Appendix A.

In this way, a system of four equations $\phi(\mathbf{X})_i = \Phi(\mathbf{X})_i, \;\; i = 1 \ldots 4$ is obtained

$$\begin{cases} s^2(C_{11} + C_{22} + 2C_{12}) = \dfrac{t\pi s^2\delta^3}{24}(3k_{n_1} + 3k_{n_2} + 4k_{t_1} + 2k_\nu) \\ s^2\, C_{11} = \dfrac{t\pi s^2\delta^3}{384}(38k_{n_1} + 6k_{n_2} + 24k_{t_1} + 4k_\nu) \\ s^2\, C_{22} = \dfrac{t\pi s^2\delta^3}{384}(6k_{n_1} + 38k_{n_2} + 24k_{t_1} + 4k_\nu) \\ 2\gamma^2\, C_{66} = \dfrac{t\pi \gamma^2\delta^3}{192}(6k_{n_1} + 6k_{n_2} + 24k_{t_1} + 4k_\nu) \end{cases} \tag{44}$$

and that solved leads to:

$$k_{n_1} = \frac{12\,(C_{11} - C_{66})}{\pi t \delta^3} \tag{45}$$

$$k_{n_2} = \frac{12\,(C_{22} - C_{66})}{\pi t \delta^3} \tag{46}$$

$$k_\nu = \frac{12\,(3C_{12} - C_{66})}{\pi t \delta^3} \tag{47}$$

$$k_{t_1} = \frac{3\,(8C_{66} - C_{11} - C_{22} - 2C_{12})}{\pi t \delta^3} \tag{48}$$

In the special case of isotropy under plane stress conditions they reduce to two independent constants

$$k_n = \frac{12\,(C_{11} - C_{66})}{\pi t \delta^3} = \frac{6E}{\pi t \delta^3 (1 - \nu)} \tag{49}$$

$$k_t = \frac{3\,(8C_{66} - 2C_{11} - 2C_{12})}{\pi t \delta^3} = \frac{6E(1 - 3\nu)}{\pi t \delta^3 (1 - \nu^2)} \tag{50}$$

whereas in plane strain

$$k_n = \frac{12\,(C_{11} - C_{66})}{\pi t \delta^3} = \frac{6E}{\pi t \delta^3 (1 + \nu)(1 - 2\nu)} \tag{51}$$

$$k_t = \frac{3\,(8C_{66} - 2C_{11} - 2C_{12})}{\pi t \delta^3} = \frac{6E(1 - 4\nu)}{\pi t \delta^3 (1 + \nu)(1 - 2\nu)} \tag{52}$$

where E and ν are the Young modulus and the Poisson's ratio of the material, respectively.

By applying Eqs. (34) and (35), a specific value is assigned to the axial and shear PD springs constants, depending on the orientation ψ of the bond. In this way the mechanical behavior of a Cauchy orthotropic material can be modeled (Diana and Casolo, 2019b). Since the conceived PD model is micropolar, the particles are characterized also by a rotational degree of freedom that is required to ensure rotational invariance (Diana and Casolo, 2019a). The microrotations and the micromoments in fact, ensure the balance of angular momentum of the peridynamic bond. The definition of a shearing deformation measure which does not account for particle's rotations instead, could lead to an incorrect description of the mechanical behavior of materials undergoing non-homogeneous deformation fields, as demonstrated by Diana (2019); Diana and Casolo (2019a). However, when referring to a Cauchy continuum the definition of an equivalent lattice model requires only two elastic moduli in isotropy (four for in-plane orthotropy), and thus the definition of a rotational spring constant k_ϑ is somewhat redundant (Diana and Casolo, 2019b). In our case, it can improve the numerical performance of the discrete approximation in the case of non-homogeneous strain conditions, insofar as it allows the description of variable axial bond forces with a reduced number of elements. It can be seen as the addition of a linear term (in the bond force between two particles) in addition to the uniform axial bond force (Casolo, 2006; 2009; Diana and Casolo, 2019b). In this sense, it can be stated that the introduction of the rotational stiffness term allows an improvement in the numerical behavior of the model implemented in situations of high strain gradient, especially in the case of coarse meshes (Diana and Casolo, 2019b). Further details and a theoretical discussion on this aspect can be found in Stakgold (1950), Casolo (2006), Ostoja-Starzewski (2002) and Diana and Casolo (2019b).

In the case of principal material directions not aligned with respect to the horizontal and vertical directions, (being $\zeta \neq 0$), Eqs. (34) and (35) can be rewritten in the general form

$$\begin{aligned} k_n(\psi - \zeta) = {} & k_{n_1}\cos^4(\psi - \zeta) + k_{n_2}\sin^4(\psi - \zeta) \\ & + 2k_\nu \sin^2(\psi - \zeta)\cos^2(\psi - \zeta) \\ & + 4k_{t_1}\sin^2(\psi - \zeta)\cos^2(\psi - \zeta) \end{aligned} \tag{53}$$

$$\begin{aligned} k_t(\psi - \zeta) = {} & k_{n_1}\sin^2(\psi - \zeta)\cos^2(\psi - \zeta) \\ & + k_{n_2}\sin^2(\psi - \zeta)\cos^2(\psi - \zeta) + \\ & - 2k_\nu \sin^2(\psi - \zeta)\cos^2(\psi - \zeta) \\ & + k_{t_1}[\cos^2(\psi - \zeta) - \sin^2(\psi - \zeta)]^2 \end{aligned} \tag{54}$$

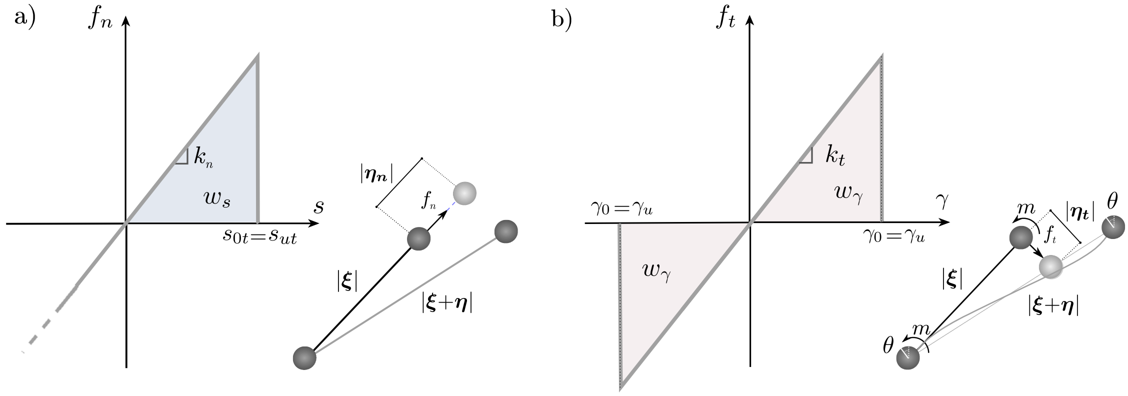

Fig. 7. Axial bond force-bond elongation $f_n - s$ (a) and shear force-shear deformation $f_t - \gamma$ (b) relationships in micropolar peridynamics.

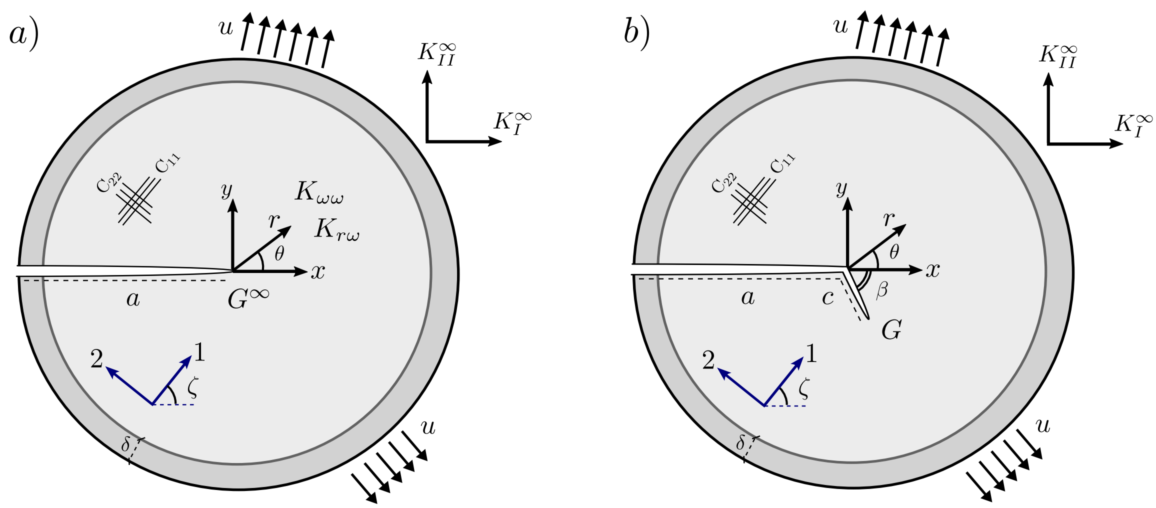

Fig. 8. Geometry and boundary conditions used for the analysis of near-tip solution in orthotropic media; (a) Semi-infinite crack; (b) Kinked crack.

Fig. 6 show that the polar plot of the normal and shear spring stiffnesses k_n and k_t have the same shape of that of C_{xx} and C_{ss}, and that they differ only of a scale factor.

2.2.1. Fracture criteria and local damage variables

The nonlocal orthotropic PD model will be applied in the next Section to the study of the stress and deformation fields in the immediate vicinity of a stationary crack-tip subjected to mixed-mode loading, and to simulate its infinitesimal extension. This paper is not concerned with the issue of which criterion should be used to dictate the direction of crack extension in an anisotropic structure. This because physically realistic crack propagation simulations will require the detailed understanding of the spatial distribution of fracture toughness in addition to possible pointwise anisotropy. The discussion is instead limited to illustrative examples that illustrate the flexibility of the PD model, when coupled with chosen crack propagation criteria, in simulating complex fracture scenarios. In fact, it will be seen that the illustrative criteria do not necessarily predict the same extension directions, the same as for the analytical criteria proposed for orthotropic continua. Before proceeding to the next Section, two illustrative crack extension criteria are described; critical stretch criterion (Silling and Askari, 2005; Diana and Casolo, 2019a), and critical bond micropotential energy criterion. We note that the former is a deformation-based criterion widely used in PD (Bobaru et al., 2015; Gerstle, 2016); the latter is an energetic criterion that relies of the previously discussed formulation. In order to make the results of the isotropic and orthotropic cases comparable, as inspired by the works of Azhdari and Nemat-Nasser (1996a), we assume that fracture resistance is uniform. The maximum stretch failure criterion (henceforth referred to as the S-criterion) adopted here assumes a perfectly brittle material (namely PMB material (Silling, 2000)), for which the elastic stretch at failure, s_{0t}, coincides with the bond ultimate stretch s_{ut}.

The ultimate tensile stretch limit s_{ut} for each bond is calculated assuming that the energy release rate of the material, G is equal to the sum of the individual works required to break every bond crossing the newly created fracture surface (divided by the new surface area) (Silling and Askari, 2005; Bobaru et al., 2015)

$$
\begin{aligned}
G &= 2\int_0^\delta \int_z^\delta \int_0^{\cos^{-1}(z/|\boldsymbol{\xi}|)} \mathrm{w}_s\, t\left|\boldsymbol{\xi}\right| \,\mathrm{d}\phi\,\mathrm{d}z\,\mathrm{d}\xi \\
&= \int_0^\delta \int_z^\delta \int_0^{\cos^{-1}(z/|\boldsymbol{\xi}|)} k_n(\psi)\left|\boldsymbol{\xi}\right| s_{ut}^2(\psi) t\left|\boldsymbol{\xi}\right| \,\mathrm{d}\phi\,\mathrm{d}\xi\,\mathrm{d}z; \\
s_{ut}^2(\psi) &= \bar{s}_{ut}^2 \frac{\overline{k_n}}{k_n(\psi)}; \rightarrow \bar{s}_{ut}^2 = \frac{4G}{\overline{k_n}\delta^4 t}
\end{aligned}
\tag{55}
$$

in which w_s here represents the micropotential energy function of the axial spring ($\overline{k_n}$ is the average value of the axial spring off-axis stiffness) when $s = s_{ut}$ and is equal to $\mathrm{w}_s = w_s|\boldsymbol{\xi}|$, where w_s is the area under the curve $f_n - s$ between $s = 0$ and $s = s_{ut}$ (i.e. the micropotential function of the axial spring). It should be noted that if assuming an isotropic surface energy in orthotropic materials, the critical stretch is function of the bond orientation

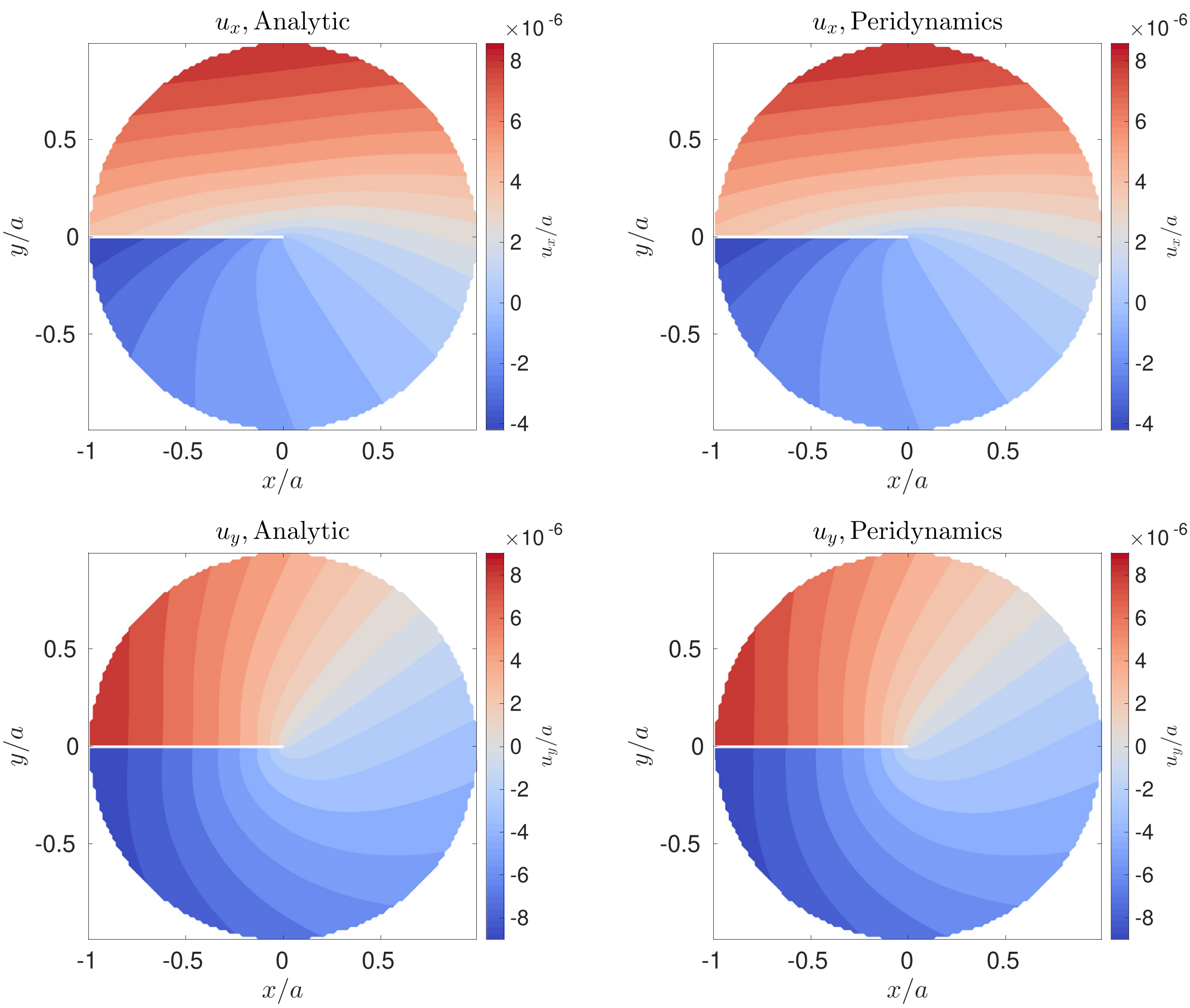

Fig. 9. Displacements map near the tip in the case of an orthotropic material characterized by $\lambda = 0.2$ $\rho = 1.2$, under Mixed-Mode I-II ($\alpha = 45^\circ$): right) Micropolar peridynamic solution; left) Analytical solution.

angle. Fig. 7 shows the axial bond force-bond elongation $f_n - s$ and shear force-shear deformation $f_t - \gamma$ relationships considered. Adopting a critical stretch criterion or S-criterion we refer to the mechanical behavior of the equivalent axial spring, because strain control is carried out exclusively on the bond stretch measure (see Fig. 7). Such a criterion was originally introduced in BBPD (Silling and Askari, 2005) for dealing with mode I brittle fracture problems. In state-based PD this criterion neglects the contribution of the deviatoric part of the deformation to the total stored elastic energy density of the bond (Dipasquale et al., 2017), and in micropolar PD it does not take into account explicitely the bond shear deformation. However, for homogeneous isotropic brittle materials at atmospheric pressure, the critical stretch criterion leads to well simulated failure conditions and realistic crack paths even in the case of pure mode II external loading (Panchadhara and Gordon, 2016; Dipasquale et al., 2014; Jiang et al., 2017), and is used in both classical and non-classical bond-based models (Dipasquale et al., 2014; Li et al., 2020), as well as in micropolar formulations (Gerstle et al., 2007; Yaghoobi and Chorzepa, 2017).

By adapting the energetic failure criterion presented by Foster et al. (2011) to the conceived MPPD model, we obtain the micropolar critical bond micropotential energy criterion (referred to as the E-criterion). Unlike the S-criterion, this criterion considers that ligament failure depends also on the bond shearing deformation. In fact, the S-criterion considers only the contribution of w_s, whereas the E-criterion takes into account w_s, w_γ and w_ϑ, where $\mathrm{w}_\gamma = w_\gamma |\boldsymbol{\xi}|$, $\mathrm{w}_\vartheta = w_\vartheta$, being w_γ the area under the curve $f_t - \gamma$ (i.e. the micropotential energy density function of the shear spring). It should be reminded that when modeling Cauchy materials, the rotational springs is not necessary and its value can be set to zero (Diana and Casolo, 2019). Since we assume here that the surface energy is isotropic, as specified in Azhdari and Nemat-Nasser (1996b,a), the critical energy parameter is the same for each bond. The critical value w_u of the bond micropotential energy $\mathrm{w} = \mathrm{w}_s + \mathrm{w}_\gamma + \mathrm{w}_\vartheta$ can be calculated for 2D cases by assuming that the fracture energy G is equal to the total work required to break all the bonds per unit of fracture surface

$$G = 2\int_0^\delta \int_z^\delta \int_0^{\cos^{-1}(z/|\xi|)} \left(\mathrm{w}_s + \mathrm{w}_\gamma + \mathrm{w}_\vartheta\right) t \left|\boldsymbol{\xi}\right| \, d\phi \, d\xi \, dz; \quad \rightarrow \mathrm{w}_u = \frac{3G}{2\delta^3 t} \tag{56}$$

Adopting this energetic criterion the rupture of the bond is activated when its stored energy density, i.e. the quantity w called elastic micropotential function reaches a critical value w_u.

In order to specify the status of a specific bond $\boldsymbol{\xi}_{ij}$ connecting two particles $\mathbf{X}_i$ and $\mathbf{X}_j$, a history-dependent scalar valued function μ is introduced (Silling and Askari, 2005), that in the case of S-

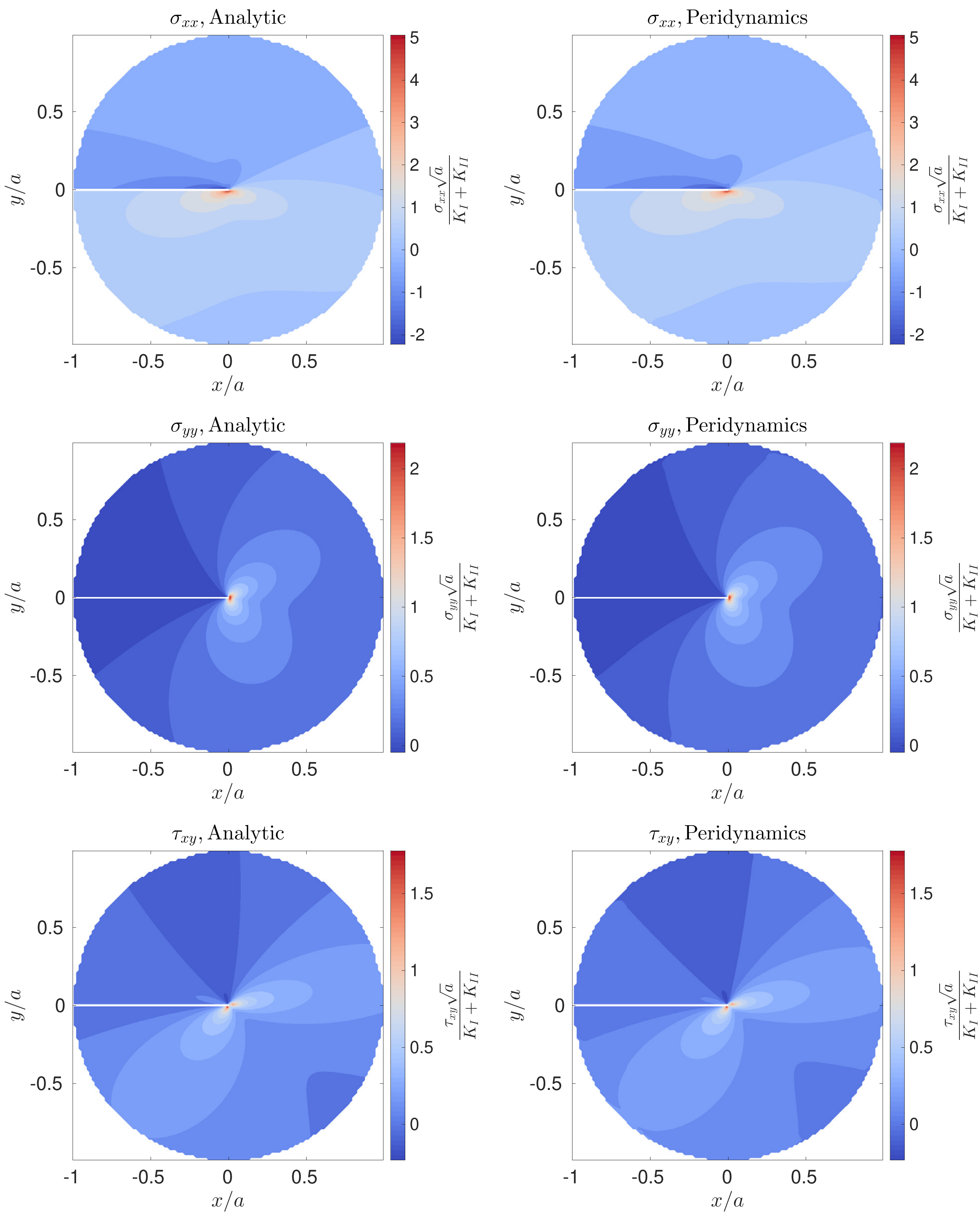

Fig. 10. Stress components map near the tip, in the case of an orthotropic material characterized by $\lambda = 0.2$ $\rho = 1.1$, under Mixed-Mode I-II ($\alpha = 45^{\circ}$): right) Micropolar peridynamic solution; left) Analytical solution.

criterion can be written as

$$\mu_S(\boldsymbol{\xi}_{ij}, t) = \begin{cases} 0 & s \geq s_{ut} \\ 1 & s < s_{ut} \end{cases} \tag{57}$$

while for the E-criterion is

$$\mu_E(\boldsymbol{\xi}_{ij}, t) = \begin{cases} 0 & \mathrm{w} \geq \mathrm{w}_u \\ 1 & \mathrm{w} < \mathrm{w}_u \end{cases} \tag{58}$$

Then, based on the function $\mu(\boldsymbol{\xi}_{ij}, t)$, a local tensile damage variable is defined and computed at each time step t and for each par-

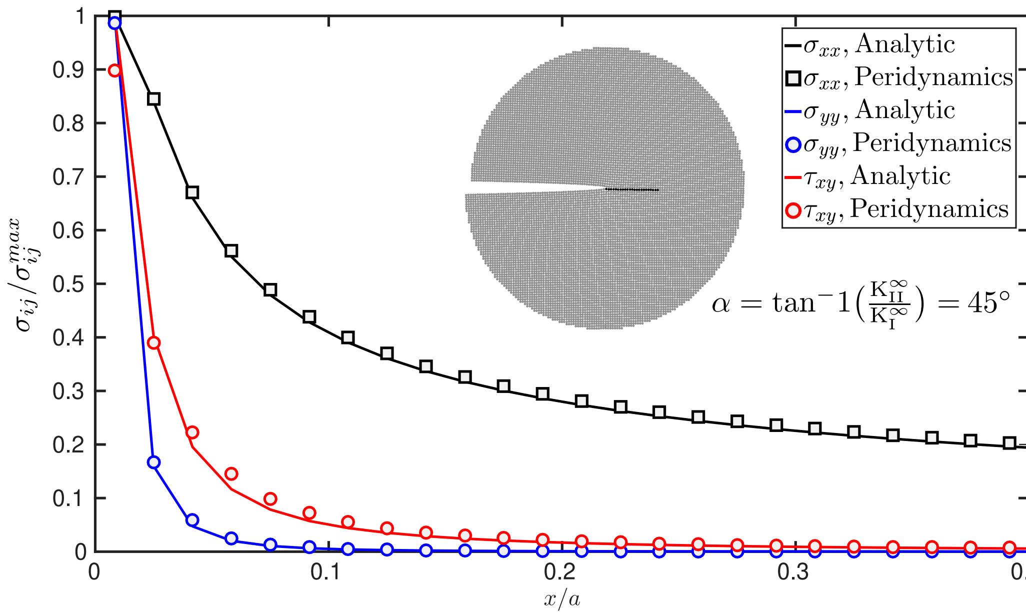

Fig. 11. Orthotropic material characterized by $\lambda = 0.2$ $\rho = 1.2$, under Mixed-Mode I-II ($\alpha = 45^\circ$). Analytical solution of LEFM in terms of stress components corresponding to the points aligned along $y = -\Delta x/2$ (i.e. the PD particles nearest to the crack line) and comparison with micropolar peridynamic solution.

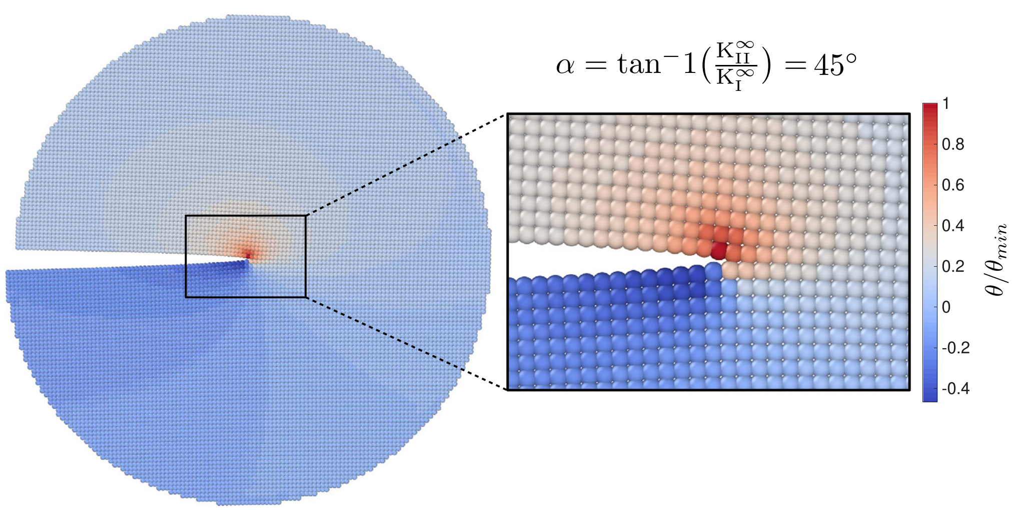

Fig. 12. Map of the particles rotations in the case of an orthotropic material characterized by $\lambda = 0.2$ $\rho = 1.1$, under Mixed-Mode I-II ($\alpha = 45^\circ$). The intensity of the rotations is higher in high-strain gradient zones such as in proximity of a crack tip.

ticle $\mathbf{X}_i$ as

$$d(\mathbf{X}_i, t) = 1 - \frac{\sum_{j=1} \mu(\boldsymbol{\xi}_{ij}, t)\Delta V_j}{\sum_{j=1} \Delta V_j} \tag{59}$$

where d is the local tensile damage whereas $\mu = \mu_S$ or $\mu = \mu_E$ depending on the specific criterion adopted. The numerator in the fraction represents the actual damaged volume of the unit cell considered, whereas the denominator is the volume of the family of particle $\mathbf{X}_i$ in the undeformed configuration.

3. Fracture mechanics of 2D orthotropic materials

Consider the plane elastostatics problem of a horizontal semi-infinite crack subjected to asymmetric loading. The material is assumed to be orthotropic, and the Cartesian coordinates x and y are chosen to coincide with principal axes of the orthotropic material. Define a local polar coordinate system (r, θ) on the crack tip.

The fourth-order differential equation representing equilibrium and compatibility produces the following characteristic equation (Lekhnitskii, 1963)

$$S_{11}\mu^4 + (2S_{12} + S_{66})\mu^2 + S_{22} = 0 \tag{60}$$

where S_{ij} are the conventional compliance matrix components (i.e. the inverse of matrix $\mathbf{C}$ in Eq. (28)). The roots of Eq. (60) are always complex or purely imaginary ($\mu_i = \mu_{ix} + \mu_{iy}, i = 1, 2$) and occur in conjugate pairs as $\mu_1, \overline{\mu}_1$ or $\mu_2, \overline{\mu}_2$[4]. The stresses and strains in the immediate vicinity of the crack tip depend on the values of the roots, as reviewed next. As in the isotropic case, the singularity of the stresses is of order $-1/2$ and the parameters that determine the amplitude of this singularity are again the mode-I and mode-II stress intensity factors (SIFs) (Chiang, 1991). For a given set of elastic constants, Eq. (60) can be solved and in turn the expression

[4] For a material reference system forming a certain angle ζ with the crack axis x, constants S_{ij}, should be modified to the new configuration and Eqs. (60) and (69) would be also modified acquiring the general form $S_{xx}\mu^4 - 2S_{xs}\mu^4 + (2S_{xy} + S_{ss})\mu^2 - 2S_{ys} + S_{yy} = 0$ (61) $p_i = S_{xx}\mu_i^2 + S_{xy} - S_{xs}\mu_i$; $q_i = S_{xy}\mu_i + \frac{S_{yy}}{\mu_i} - S_{xs}$ (62)

Table 1
Material moduli defined in the material reference system and corresponding to the four orthotropic and isotropic materials considered.

Material	C_{11} (MPa)	C_{12} (MPa)	C_{22} (MPa)	C_{66} (MPa)	λ	ρ
1, Isotropy	20,600	3500	20,600	8550	1	1
2, Degenerate orthotropy	16,070	743	803	5330	2	1
3, Cubic symmetry	8000	0	8000	2000	1	2
4, General orthotropy	33,000	730	7320	6300	0.2	1.2

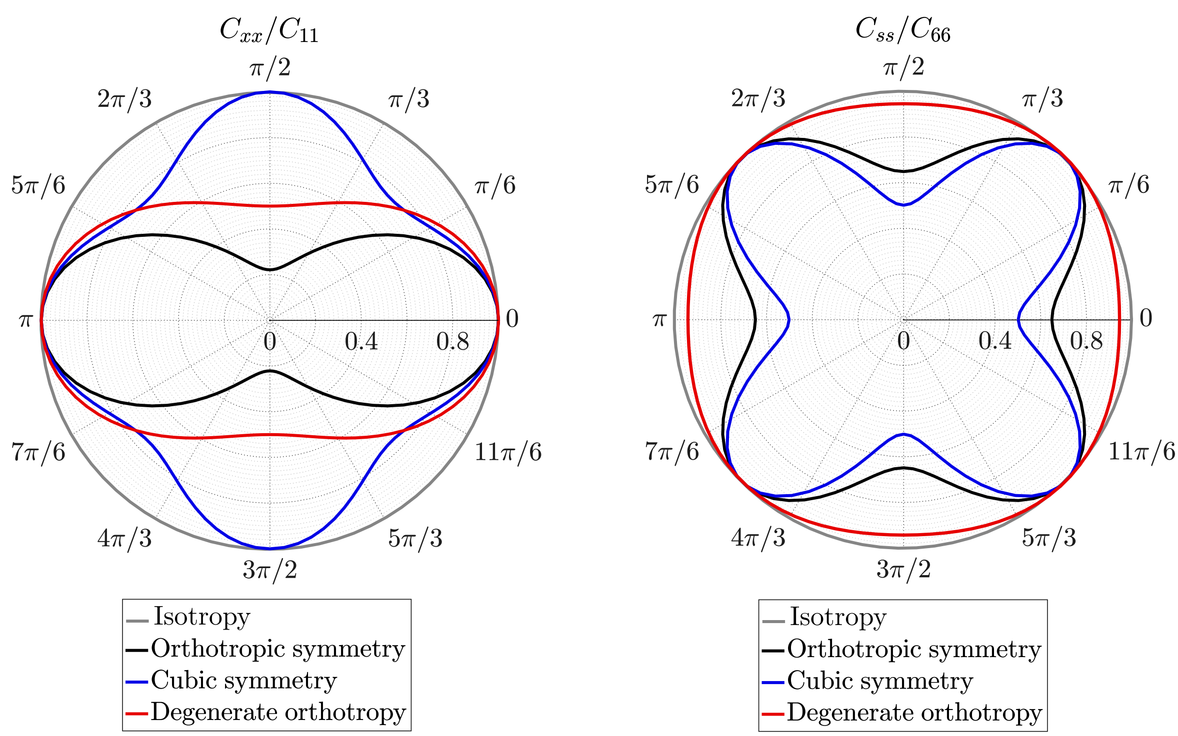

Fig. 13. Off-axis C_{xx} and C_{ss} material moduli corresponding to the four orthotropic and isotropic materials considered.

of the displacements and stress field at small distances from the crack tip can be written as (Sih et al., 1965)

$$u_x = K_{\mathrm{I}}^{\infty}\sqrt{\frac{2r}{\pi}}\,\mathrm{Re}\left[\frac{1}{\mu_1-\mu_2}\left\{\mu_1 p_2\sqrt{\cos\theta+\mu_2\sin\theta} - \mu_2 p_1\sqrt{\cos\theta+\mu_1\sin\theta}\right\}\right] + K_{\mathrm{II}}^{\infty}\sqrt{\frac{2r}{\pi}}\,\mathrm{Re}\left[\frac{1}{\mu_1-\mu_2}\left\{p_2\sqrt{\cos\theta+\mu_2\sin\theta} - p_1\sqrt{\cos\theta+\mu_1\sin\theta}\right\}\right] \tag{63}$$

$$u_y = K_{\mathrm{I}}^{\infty}\sqrt{\frac{2r}{\pi}}\,\mathrm{Re}\left[\frac{1}{\mu_1-\mu_2}\left\{\mu_1 q_2\sqrt{\cos\theta+\mu_2\sin\theta} - \mu_2 q_1\sqrt{\cos\theta+\mu_1\sin\theta}\right\}\right] + K_{\mathrm{II}}^{\infty}\sqrt{\frac{2r}{\pi}}\,\mathrm{Re}\left[\frac{1}{\mu_1-\mu_2}\left\{q_2\sqrt{\cos\theta+\mu_2\sin\theta} - q_1\sqrt{\cos\theta+\mu_1\sin\theta}\right\}\right] \tag{64}$$

$$\sigma_{xx} = \frac{K_{\mathrm{I}}^{\infty}}{\sqrt{2\pi r}}\,\mathrm{Re}\left[\frac{\mu_1\mu_2}{\mu_1-\mu_2}\left\{\frac{\mu_2}{\sqrt{\cos\theta+\mu_2\sin\theta}} - \frac{\mu_1}{\sqrt{\cos\theta+\mu_1\sin\theta}}\right\}\right] + \frac{K_{\mathrm{II}}^{\infty}}{\sqrt{2\pi r}}\,\mathrm{Re}\left[\frac{1}{\mu_1-\mu_2}\left\{\frac{\mu_2^2}{\sqrt{\cos\theta+\mu_2\sin\theta}} - \frac{\mu_1^2}{\sqrt{\cos\theta+\mu_1\sin\theta}}\right\}\right] \tag{65}$$

$$\sigma_{yy} = \frac{K_{\mathrm{I}}^{\infty}}{\sqrt{2\pi r}}\,\mathrm{Re}\left[\frac{1}{\mu_1-\mu_2}\left\{\frac{\mu_1}{\sqrt{\cos\theta+\mu_2\sin\theta}} - \frac{\mu_2}{\sqrt{\cos\theta+\mu_1\sin\theta}}\right\}\right] + \frac{K_{\mathrm{II}}^{\infty}}{\sqrt{2\pi r}}\,\mathrm{Re}\left[\frac{1}{\mu_1-\mu_2}\left\{\frac{\mu_2^2}{\sqrt{\cos\theta+\mu_2\sin\theta}} - \frac{\mu_1^2}{\sqrt{\cos\theta+\mu_1\sin\theta}}\right\}\right] \tag{66}$$

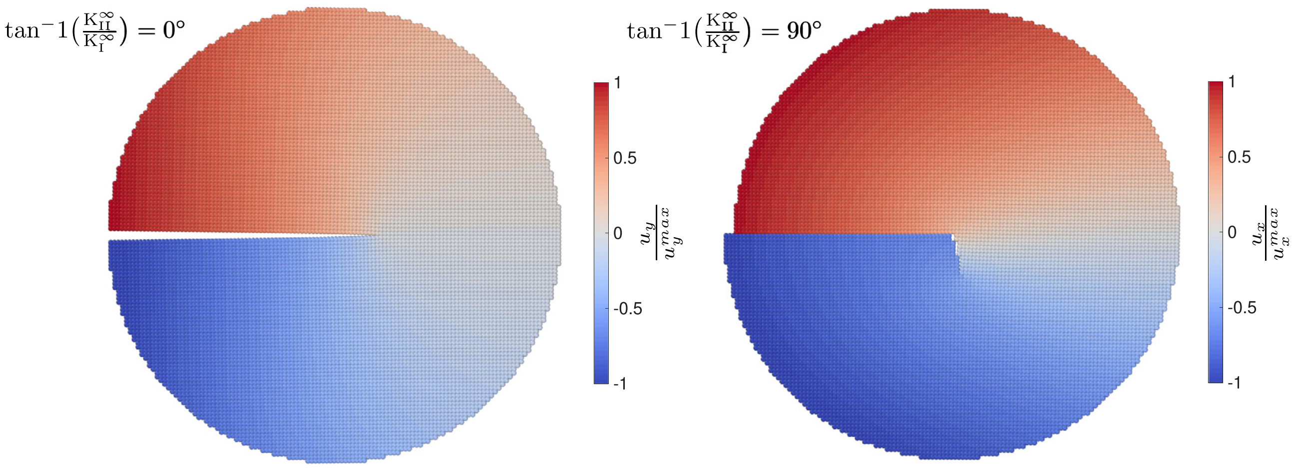

Fig. 14. MAT 1, Isotropic: Crack kinking corresponding to a pure mode I ($\alpha = 0°$) and pure mode II ($\alpha = 90°$), adopting the peridynamic S-criterion (map of vertical and horizontal displacements).

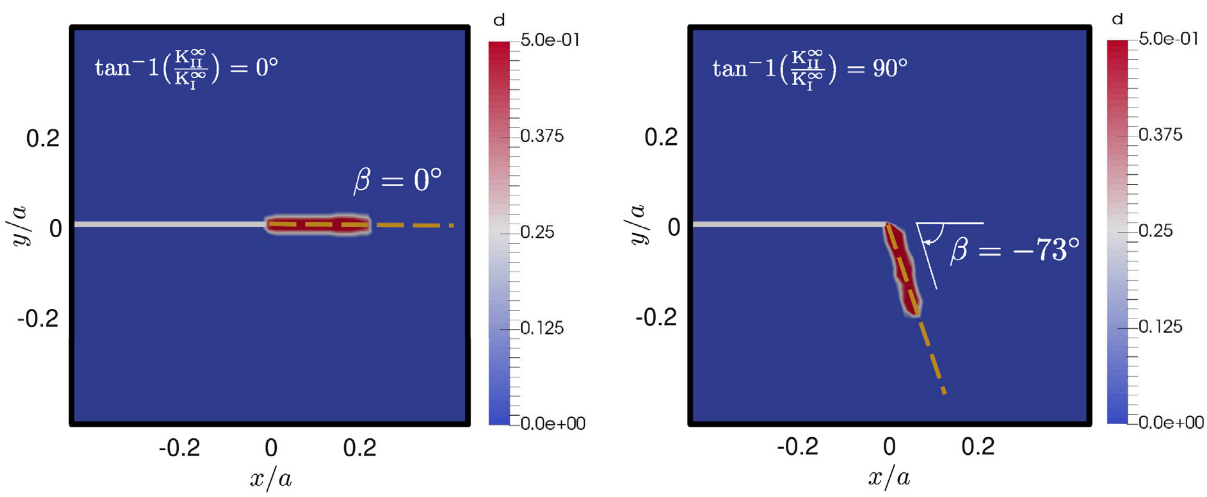

Fig. 15. MAT 1, Isotropic: Crack kinking corresponding to a pure mode I ($\alpha = 0°$) and pure mode II ($\alpha = 90°$), adopting the peridynamic S-criterion (damage map).

$$\tau_{xy} = \frac{K_I^{\infty}}{\sqrt{2\pi r}} \mathrm{Re}\left[\frac{\mu_1\mu_2}{\mu_1-\mu_2}\left\{\frac{1}{\sqrt{\cos\theta+\mu_1\sin\theta}} - \frac{1}{\sqrt{\cos\theta+\mu_2\sin\theta}}\right\}\right] + \frac{K_{II}^{\infty}}{\sqrt{2\pi r}} \mathrm{Re}\left[\frac{1}{\mu_1-\mu_2}\left\{\frac{\mu_1}{\sqrt{\cos\theta+\mu_1\sin\theta}} - \frac{\mu_2}{\sqrt{\cos\theta+\mu_2\sin\theta}}\right\}\right] \tag{67}$$

where and Re denotes the real part of the corresponding statement and p_i, q_i for $i = 1, 2$ are given by

$$p_i = S_{11}\mu_i^2 + S_{12} \tag{68}$$

$$q_i = S_{12}\mu_i + \frac{S_{22}}{\mu_i} \tag{69}$$

Suo (1990) has emphasized the importance to fracture mechanics analysis of the fact that the stress and deformation in plane problems depends only on two non-dimensional elastic parameters λ and ρ defined as

$$\lambda = \frac{S_{11}}{S_{22}} \quad \text{and} \quad \rho = \frac{2S_{12}+S_{66}}{2\sqrt{S_{11}S_{22}}} \tag{70}$$

These parameters measure the anisotropy of the material in the sense that $\lambda = 1$, $\rho \neq 1$ corresponds to cubic symmetry, $\lambda \neq 1$, $\rho = 1$ is referred to degenerate orthotropy, and $\lambda = \rho = 1$ corresponds to the case of isotropy. In the most general case, orthotropic materials are characterized by $\lambda \neq 1$, $\rho \neq 1$. Positive definiteness of the strain energy density function implies $\lambda > 0$ and $\rho > -1$. In what follows, the aforementioned parameters for characterizing the orthotropic materials under consideration are used.

The ability of the conceived MPPD formulation in characterizing the fields surrounding a crack-tip is illustrated for the case of a material characterized by $\lambda = 0.2$ and $\rho = 1.2$. The universal nature of the asymptotic fields near the crack front eliminate the need to model finite geometry specimens and specific loadings when studying the near-crack front region. The dominance of the asymptotic solution allows a boundary layer analysis involving only the near-front region, to which the effects of the loading and specimen geometry are transmitted by prescribing to its boundary the displacement field from this elastic solution and the associated stress intensity factors (Dontsova and Ballarini, 2017; Paris, 2014). This 'boundary layer' analysis greatly reduces the simulation volume size, and allows the results to be applied to finite geome-

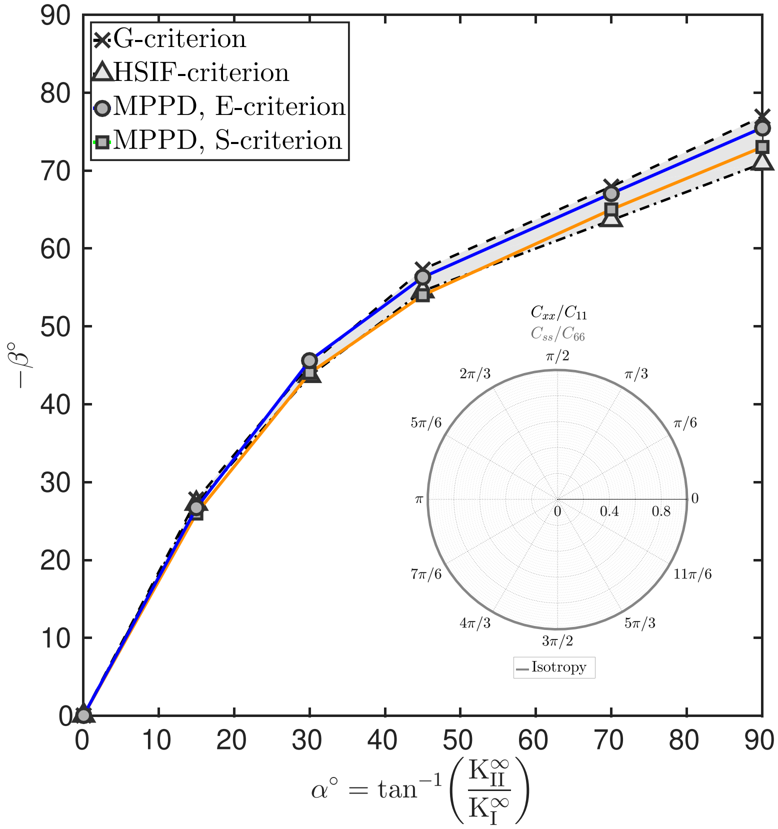

Fig. 16. MAT 1, Isotropic: Kinking angles corresponding to general Mixed-mode loadings and computed adopting the MPPD S-criterion and E-criterion.

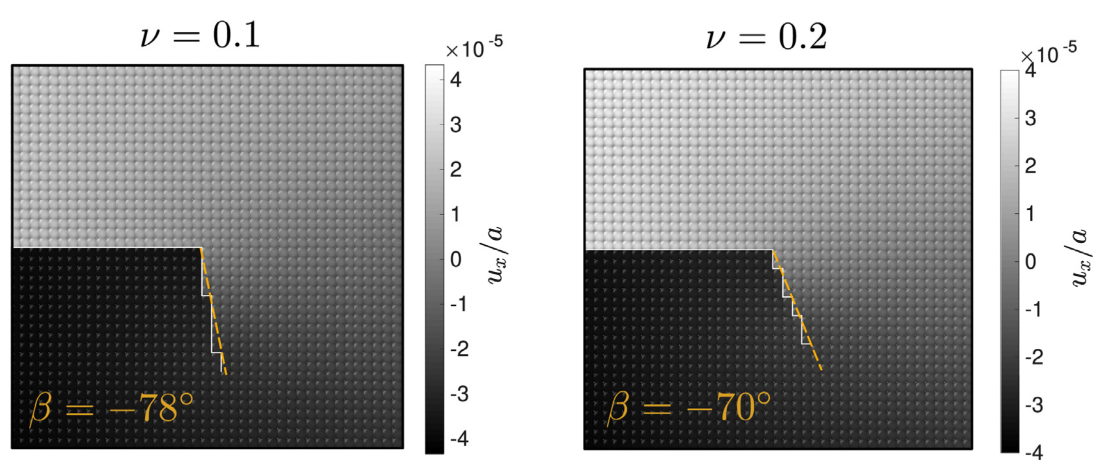

Fig. 17. MAT 1, Isotropic, Mode II loading conditions: Computed kinking angles adopting the peridynamic S-criterion with $\nu = 0.1$ and $\nu = 0.2$.

try configurations whose near-crack front regions are dominated by their own (known) stress intensity factors (Dontsova and Ballarini, 2017). The semi-infinite crack is assumed horizontal, $\zeta = 0$, the mixity mode angle $\alpha = \tan^{-1}(K_{II}^\infty/K_I^\infty) = 45^\circ$, and the discretization adopted is characterized by $\delta = 0.05a$ and $m = 3.2$, values that represent a good compromise between the accuracy of the elastic local solution and the computational effort, as demonstrated by previous works carried out by the authors (Diana and Casolo, 2019a; Ballarini et al., 2018). The performed analysis setup is shown schematically in Fig. 8(a), where a circular shape of diameter $2a$, unit thickness, and crack of length a (note that this model represents a crack whose length is infinite compared to the size of the modeled region), is subjected to displacement boundary conditions along its entire circumference corresponding to Eqs. (63) and (64). Figs. 9–12 show that the stress and displacements computed using the conceived micropolar formulation are in excellent agreement with the analytical values. For additional details regarding the validation of the model in the case of general homogeneous and non-homogeneous in-plane deformation fields, and in the case of material reference system not aligned with the Cartesian axes, see Diana (2019). When the magnitude of the prescribed far-field displacements given by Eqs. (63) and (64) increases so that the crack extension criteria is satisfied, the 'pre-existing' crack of Fig. 8(a) could extend in a direction dictated by a yet another physically based criterion. Define the direction of an infinitesimal extension by the angle β, which depends on the spatial distribution of the fracture toughness (and possibly on its anisotropy) and on K_{II}^∞ and K_I^∞. Numerous extension directions have been pro-

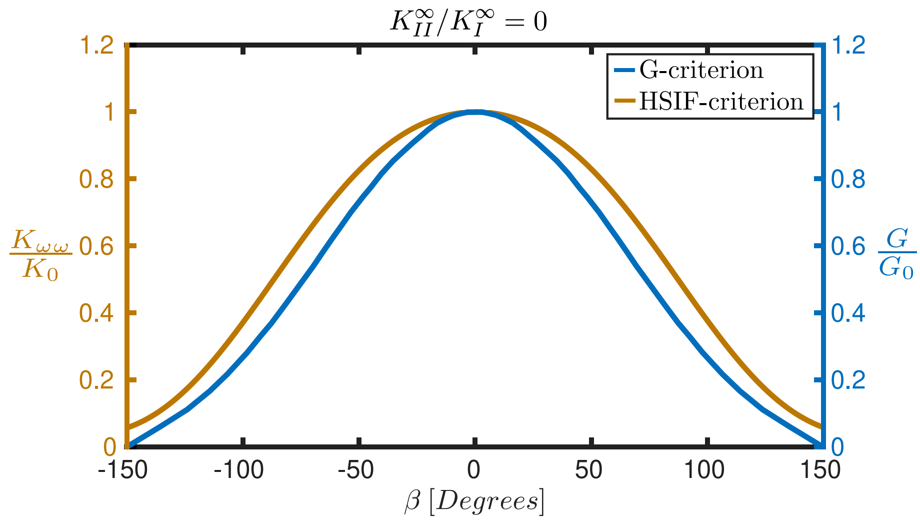

Fig. 18. MAT 2, Degenerate orthotropy (Mode I): Variation of HSIF and G versus the kink angle β. The results are normalized by K_0 ($K_{\omega\omega}(\omega=0)$) and G_0 (the energy-release rate for collinear extension of the main crack.).

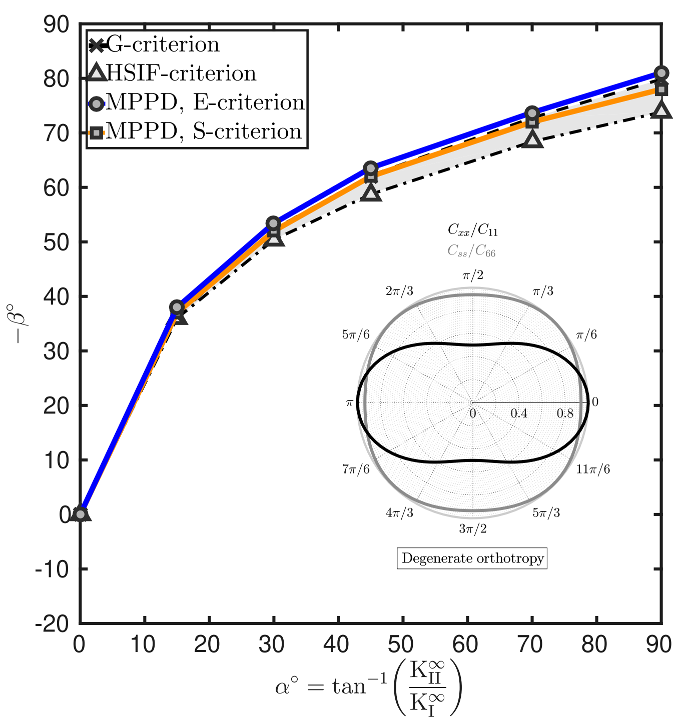

Fig. 19. MAT 2, Degenerate orthotropy: Kinking angles corresponding to general Mixed-mode loadings and computed adopting the MPPD S-criterion and E-criterion.

posed (Khan and Khraisheh, 2000). The most commonly used and accepted criteria can be grouped under two headings: stress-based (or K-based) criteria (Erdogan and Sih, 1963; Williams and Ewing, 1984) and energy-based criteria (Wu, 1978; Griffith, 1920), in which the critical condition refers to one of the extremum of the stated parameter (stress, stress intensity factors or energy).

In this paper, we refer to the maximum hoop stress intensity factor criterion (HSIF-criterion) (Azhdari and Nemat-Nasser, 1996b; Erdogan and Sih, 1963) and the maximum energy release rate fracture criterion (G-criterion) (Azhdari and Nemat-Nasser, 1996a; Wu, 1978). The former relies on the definition of two stress intensity factors; the so-called 'hoop' (HSIF) and 'shear' (SSIF) stress intensity factors, respectively (Huajian and Cheng-Hsin, 1992; Azhdari and Nemat-Nasser, 1996b). The first involves the circumferential stress and the latter the shear stress. According to this criterion, the crack will extend along a path whose tangent forms an angle, $\beta_{K_{\omega\omega}^{\max}}$, perpendicular to the maximum circumferential (hoop) stress. For anisotropic materials, HSIF and SSIF are more convenient quantities than the commonly used Modes I and II stress intensity factors, since HSIF and SSIF uncouple the Modes I and II on planes at suitable angles relative to the main crack (Azhdari and Nemat-Nasser, 1996b; Obata et al., 1989). The HSIF and SSIF can be written as a linear combination of the apparent stress intensity factors, K_{I}^{∞} and K_{II}^{∞} as

$$K_{\omega\omega}=K_{11}K_I^{\infty}+K_{12}K_{II}^{\infty},\quad K_{r\omega}=K_{21}K_I^{\infty}+K_{22}K_{II}^{\infty} \tag{71}$$

where

$$\begin{aligned}
K_{11}&=\mathrm{Re}\left[\frac{1}{\mu_2-\mu_1}\left\{\mu_2(c+\mu_1 s)^{3/2}-\mu_1(c+\mu_2 s)^{3/2}\right\}\right]\\
K_{12}&=\mathrm{Re}\left[\frac{1}{\mu_2-\mu_1}\left\{(c+\mu_1 s)^{3/2}-(c+\mu_2 s)^{3/2}\right\}\right]\\
K_{21}&=\mathrm{Re}\left[\frac{1}{\mu_2-\mu_1}\left\{\mu_2(c+\mu_1 s)^{1/2}(s-\mu_1 c)\right.\right.\\
&\qquad\left.\left.-\mu_1(c+\mu_2 s)^{1/2}(s-\mu_2 c)\right\}\right]\\
K_{22}&=\mathrm{Re}\left[\frac{1}{\mu_2-\mu_1}\left\{(c+\mu_1 s)^{1/2}(s-\mu_1 c)\right.\right.\\
&\qquad\left.\left.-(c+\mu_2 s)^{1/2}(s-\mu_2 c)\right\}\right]
\end{aligned} \tag{72}$$

Hence, the initial crack will kink at the angle β that maximizes the functional $K_{\omega\omega}$ (i.e. HSIF). Along the direction for which HSIF is extremum, SSIF is zero. Therefore, the maximum-$K_{\omega\omega}$ and the zero-$K_{r\omega}$ fracture criteria yield identical results.

The maximum energy release rate criterion (G criterion) stems from the principle of minimum potential energy. The formal definition of the strain energy release rate, G, refers to the change in potential energy with respect to an infinitesimal crack extension. In the absence of additional work, this can be equated with a change in the work necessary to virtually close the crack. A finite kink energy release rate in two dimensions is defined by, $G=\partial W/\partial c$, where c is the kink length.

According to the G-criterion (He and Hutchinson, 1989), the crack will propagate along the direction β, that maximizes the energy release rate. This direction will be referred to as the $G_{\max}$ angle, $\beta_{G_{\max}}$ (Becker et al., 2001). The energy-release rate at the in-

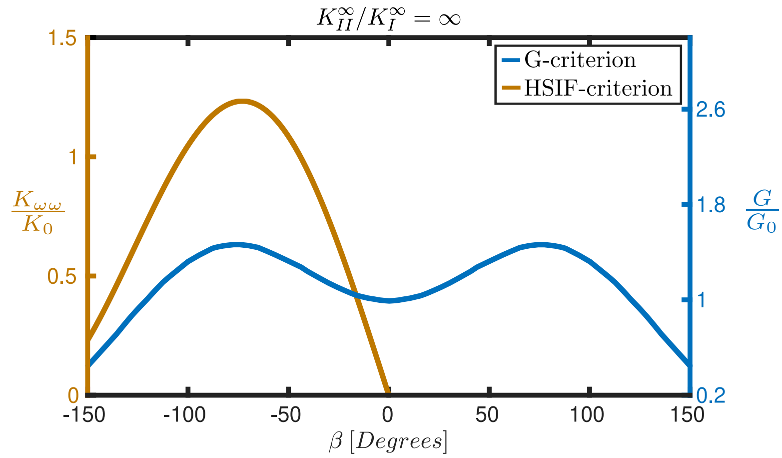

Fig. 20. MAT 3, Cubic symmetry (Mode II): Variation of HSIF and G versus the kink angle β.

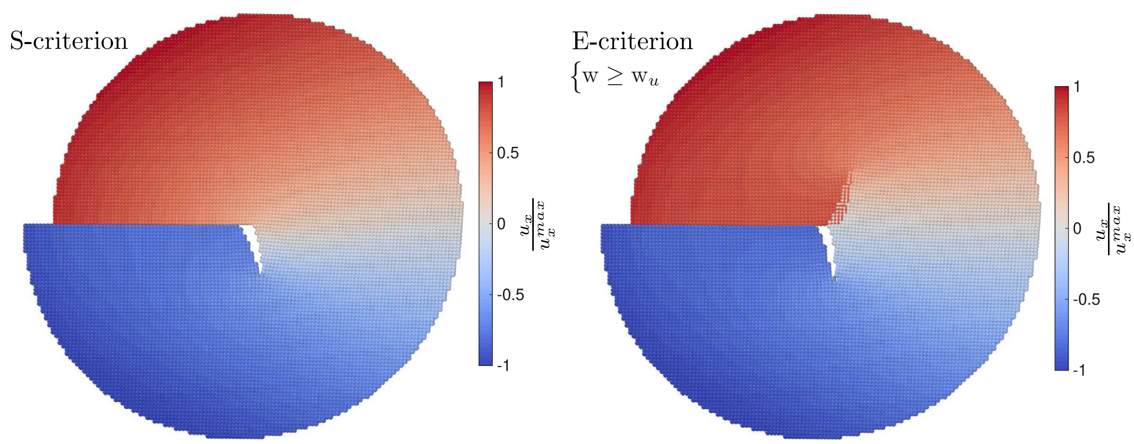

Fig. 21. MAT 3, Cubic symmetry (Mode II): Kinked crack according to S-criterion and standard E-criterion (without any conditions on the sign of the bond stretch). Similarly to what predicted by the G-criterion, according to the standard E-criterion crack branching occurs because the fracture criterion offers almost equal opportunity for the crack to open in two directions. The negative kinking angle is associated with a tensile stress whereas the positive kinking angle is associated with a compressive stress.

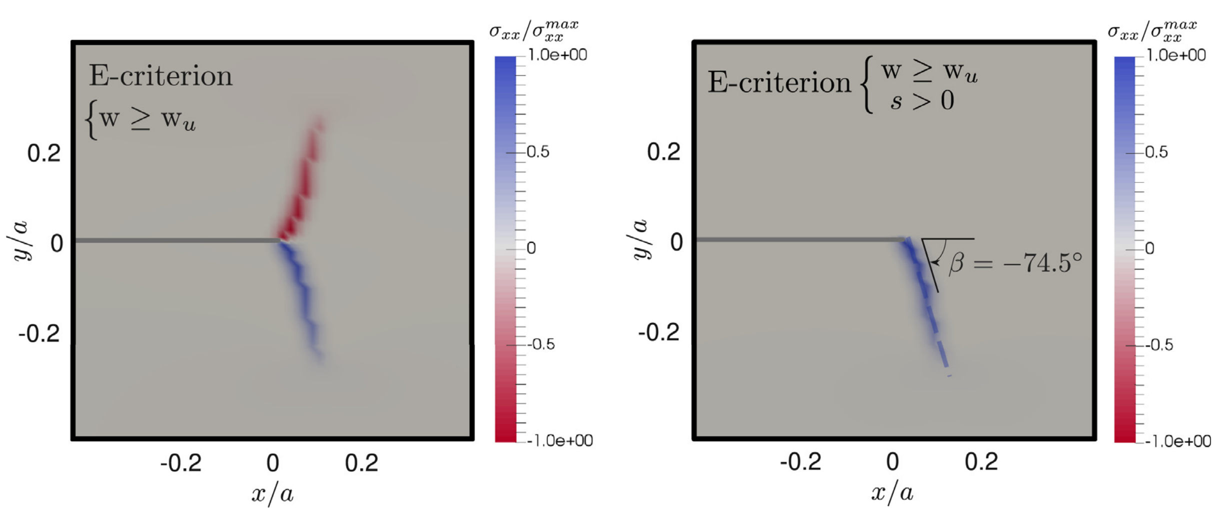

Fig. 22. MAT 3, Cubic symmetry: Crack kinking predictions adopting the standard E-criterion and the E-criterion with the condition of positiveness of the bond stretch to avoid crack propagation in compressive zones (σ_{xx} stress map).

ception of kinking is given by

$$G=\frac{1}{4\sqrt{\pi}}\sum_{k=1}^{N}\int_{s_{2k-1}}^{s_{2k+1}}[K_{\omega\omega}V^k(s)+K_{r\omega}U^k(s)]\frac{1}{\sqrt{s+1}}\,ds \tag{73}$$

This equation gives the energy-release rate due to the nucleation of an infinitesimally small kink along the angle β and gives the same results of the commonly used energy-release-rate formula, namely the modified Irwin formula (Sih et al., 1965). The numerical routine that is needed to perform the above integration is based on the method that models a kink as a continuous distribution of edge dislocations (Obata et al., 1989). The kink length is partitioned in N subintervals, s is the abscissa defined along the crack line and $U(s)$,

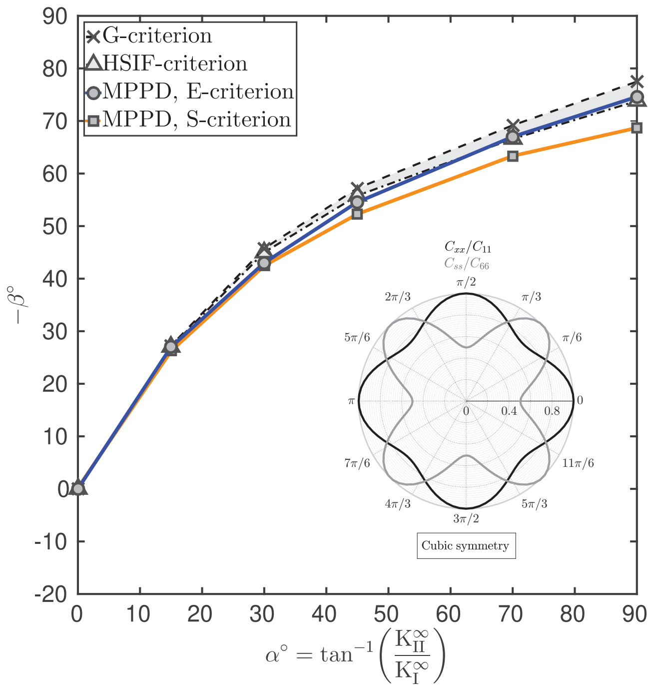

Fig. 23. MAT 3, Cubic symmetry: Kinking angles corresponding to general Mixed-mode loadings and computed adopting the MPPD S-criterion and E-criterion.

$V(s)$ are the kink opening displacements in the kink and normal to the kink directions which can be derived from the dislocation density functions $b_x(s)$ and $b_y(s)$ (Azhdari and Nemat-Nasser, 1996a). At this point, the remaining problem is to seek the theoretical kinked crack angles $\beta_{K_{\omega\omega}^{\max}}$, $\beta_{G^{\max}}$ according to the aforementioned criteria, and compare them with those resulting from peridynamic simulations, for an assigned material and mode mixity, $\alpha = K_{II}^\infty/K_I^\infty$ angle. As stated previously, the extension direction may be influenced also by potential anisotropy and spatially random distribution of the surface energy of the material. For the purposes of this discussion, and in order to guarantee consistency among the results compared, illustrative examples assume always isotropic surface energy as specified in Azhdari and Nemat-Nasser (1996b,a). In fact, here we want here to investigate in which ways the elastic anisotropy of the material and the the specific features of the failure criteria considered, can influence the kinking phenomenon.

The same conditions are considered for the numerical micropolar peridynamic simulations, which follow an implicit non-linear quasi-static scheme in displacement control (Ni et al., 2019).

Assuming that the plane of the main crack is the principal plane of orthotropy xz, we consider three different orthotropic materials characterized by an almost degenerate orthotropy ($\lambda = 2$, $\rho = 1$), cubic symmetry ($\lambda = 1$, $\rho = 2$), and general orthotropy or orthotropic symmetry ($\lambda = 0.2$, $\rho = 1.2$). An isotropic material under plane stress conditions is also considered in this study (Fig. 13). For each material, several K_{II}^∞/K_I^∞ mode mixity ratios are studied, and then the crack kinking angles β are determined adopting both the PD bond failure criteria described in the previous section (S-criterion and E-criterion).

3.1. Isotropy

In isotropic materials, the commonly used maximum HSIF and maximum energy release rate G fracture criteria are known to lead, to the first order in the kink angle, to the same extension directions.

The largest discrepancy between the two theories is associated with pure shear loading (the most asymmetric case for isotropic materials) (Azhdari and Nemat-Nasser, 1996a); for this case the corresponding equations show that the crack would kink at angles of about -71° and -77°, according to maximum HSIF and maximum energy-release rate, respectively. In the specific case of the isotropic material (MAT 1) under plane-stress conditions ($\nu = 0.17$, an average value between 0 and 1/3, see Table 1), the numerically simulated MPPD kinking angles β are in good agreement with the analytical values predicted by G-criterion and HSIF-criterion, as shown in Figs. 14–16. Both the peridynamic failure criteria considered in this study lead to consistent predictions of the crack initiation angles and as in the case of G and HSIF fracture criteria the greatest dissimilarity among the computed values of β corresponds to the case of pure Mode II loading (Fig. 16). It should be emphasized that in the case of pure mode II loading, the fracture angles are well simulated even adopting the maximum axial stretch criterion, and this can be explained by the fact that in isotropic materials the crack front is expected to be always locally associated with Mode I or, in other words, the material fails in a local opening mode. However, according to the G-criterion and to the HSIF-criterion, the crack kinking angle is not influenced by the

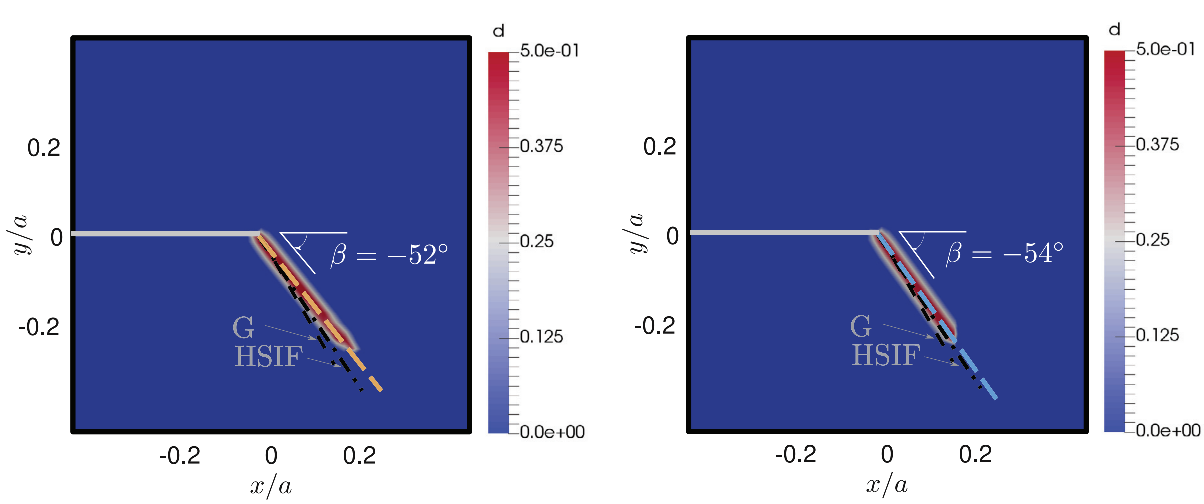

Fig. 24. MAT 3, Cubic symmetry: Crack kinking angles corresponding to a Mixed-Mode I-II ($\alpha = 45^\circ$) and computed adopting the MPPD S-criterion (left) and E-criterion (right).

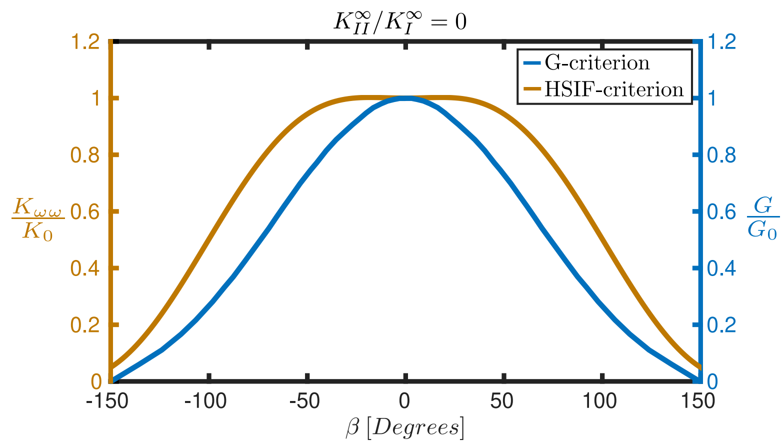

Fig. 25. MAT 4, General orthotropy (Mode I): Variation of HSIF and G versus the kink angle β.

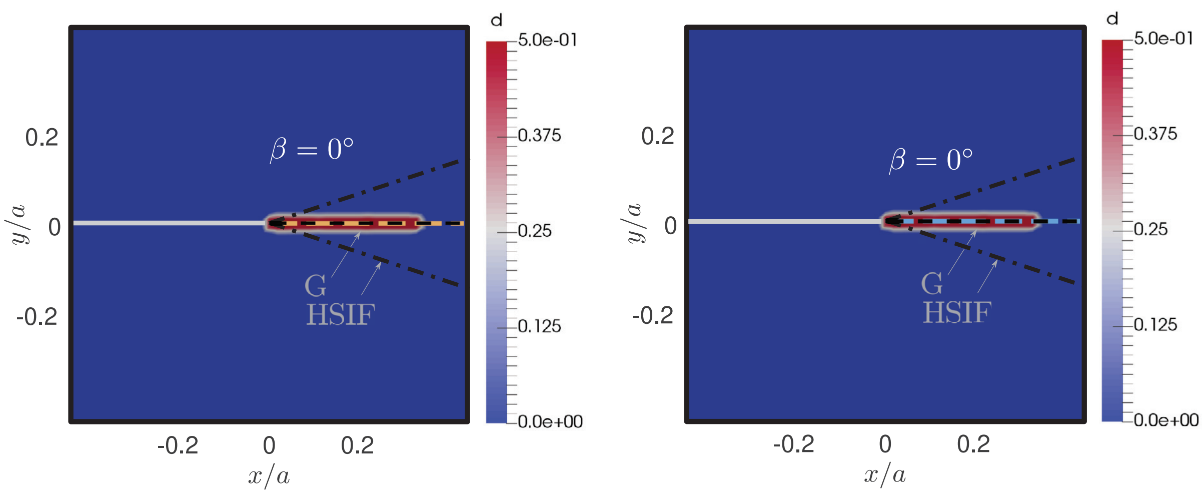

Fig. 26. MAT 4, General orthotropy: Crack kinking angles corresponding to a pure Mode I ($\alpha = 0°$) and computed adopting the MPPD S-criterion (left) and E-criterion (right). Dashed black lines indicate the analytical predictions of the HSIF and G criteria.

specific value of the Poisson's ratio of the material. Examples of fracture criteria for isotropic materials that take into account the effect of the Poisson's ratio ν, are the minimum strain energy density (SED) criterion proposed by Sih (1974) and the maximum tangential strain (MTSN) criterion proposed by Chang (1981), even if these criteria led to very different predictions. Regarding the PD failure criteria, it is noted an influence of the Poisson's ratio of the material on the computed kinking angles especially in the case of peridynamic S-criterion and pure Mode II loading. Fig. 17 shows that the Poisson's ratio affects the results and in particular, the larger is its value, the smaller is the magnitude of the resulting kinking angle. In any case the computed angles are always consistent with those corresponding to G-criterion and HSIF-criterion.

3.2. Orthotropy

Regarding the pure Mode I case, it is observed that the energy release rate G has always (if the material reference system is aligned with the horizontal) an absolute maximum at $\beta = 0°$. The HSIF has an absolute maximum at the same angle, but only for $r = E_{11}/E_{22} \leq 4$, as in the case of MAT 2 (see Fig. 18) and MAT 3. Considering first the degenerate orthotropic material (MAT 2), both the MPPD S-criterion and E-criterion, predict a simple extension of the main crack under pure Mode I loading, hence the same $\beta = 0$ as the analytical fracture criteria. Moreover, even for general Mixed-Mode conditions, their predictions are very similar and lead to kinking angles that are in good agreement with those corresponding to the analytical values (Fig. 19). This is not surprising, also considering that in degenerate orthotropic materials the orthotropic shear factor $\rho = 1$, and its off-axis shear modulus diagram is similar to that of isotropic materials. For this reason, a peridynamic failure criterion that takes into account also the shear component of the bond micropotential energy function, as the E-criterion does, seems to not give further conditions for the main crack to kink at a relatively different angle with respect to that of S-criterion.

However, the K-based and G-based fracture criteria, in general, do not predict the same angle for crack kinking (Azhdari and Nemat-Nasser, 1996a), and their differences appear more evident in orthotropic materials.

It should be also be noted that in the case of pure shear, the G-curve possess two maxima associated with opposite kinking angles, and one local minimum point in between. In other words, according to G-criterion, the main crack would branch at $\beta = \pm k$ under pure Mode II loading (Fig. 20).

By considering the fact that cracks generally propagate into tension (but not compression) zones, it is clear that the interpretation of the fracture mode and the branch angle must be accompanied by the consideration of the HSIF at the maxima of the G-curve. In the case of $\alpha = 90°$, HSIF is positive when β is negative and therefore, fracture may occur only for negative angles β, as shown in Fig. 20.

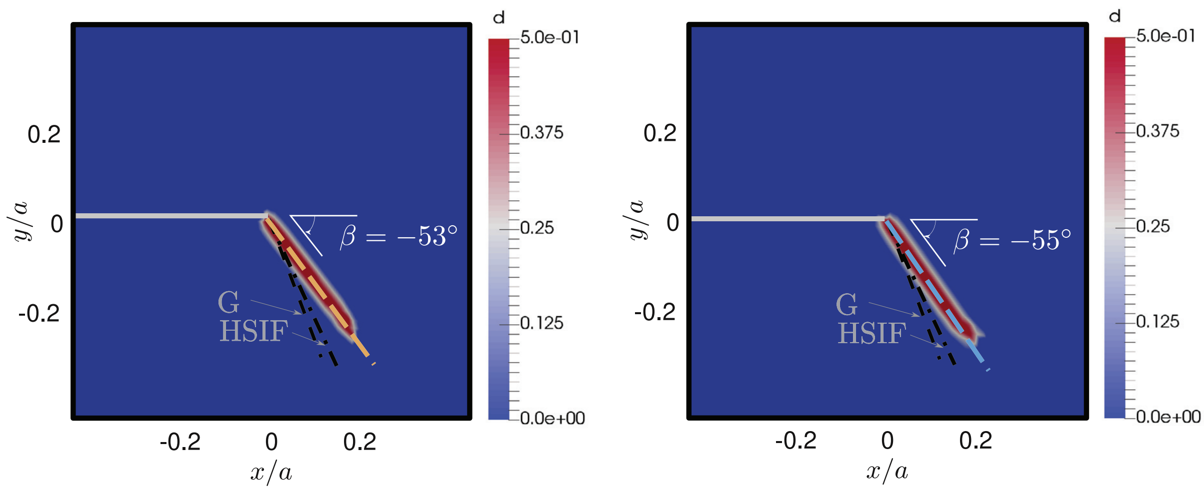

Fig. 27. MAT 4, General orthotropy: Crack kinking angles corresponding to a Mixed-Mode I-II ($\alpha = 45^\circ$) and computed adopting the MPPD S-criterion (left) and E-criterion (right).

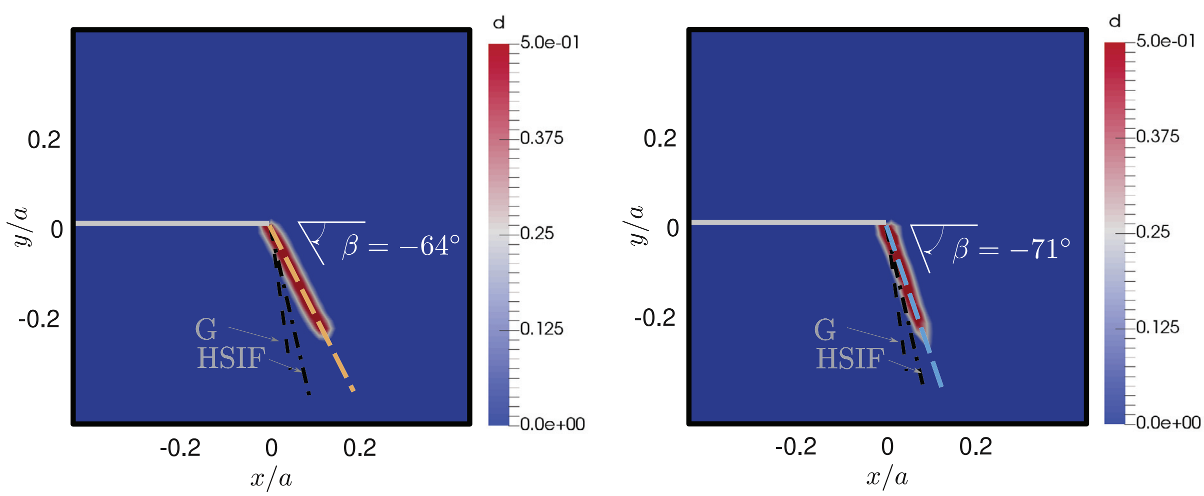

Fig. 28. MAT 4, General orthotropy: Crack kinking angles corresponding to a pure Mode II ($\alpha = 90^\circ$) and computed adopting the MPPD S-criterion (left) and E-criterion (right). Dashed black lines indicate the analytical predictions of the HSIF and G criteria.

For this reason we don't consider theoretical G-criterion kinking angles associated with compression, since the G-fracture criterion (by itself) is not sufficient for describing properly the phenomenon of kinking (Azhdari and Nemat-Nasser, 1996a). In the following figures the kinking direction corresponding to positive angle predicted by the G-criterion are not reported. Similarly to the predictions of the G-criterion, in PD simulations under mode II and performed adopting the energetic E-criterion, crack branching occurs for all the materials considered because the fracture criterion offers almost equal opportunity for the crack to open in two directions. The negative kinking angle is associated with a tensile stress whereas the positive kinking angle is associated with a compressive stress, as shown in Fig. 21 which reports the case of MAT 3 (cubic symmetry). To avoid this behavior when dealing with the MPPD E-criterion, we superimpose a further condition of positiveness of the bond stretch to determine if a ligament fails or not under a certain load. In other words, only those bonds for which the stretch is not negative, are affected by the degradation function μ_E (see Fig. 22).

This is in a certain sense similar to the tension-compression split of the stored energy functional usually considered in phase field models (Miehe et al., 2010). In fact, the standard phase-field approach cannot discriminate between the asymmetric tensile and compressive behavior, and it predicts identical cracking in regions under compression, which is not realistic for brittle and quasi-brittle fracture (Bourdin et al., 2000). Nevertheless for general mixed-Mode loading the analytical kinking angles appear to be well approximated by the micropolar peridynamic E-criterion (Figs. 21–23).

When considering instead a general orthotropic material, it is noted that under Mode I, HSIF shows one local minimum and two symmetrically located maxima if $r = E_{11}/E_{22} \geq 4$ (as in the case of MAT 4). This means that, similarly to the G-criterion under pure shear, the HSIF-criterion predicts that the main crack of MAT 4 branches in two directions of $\beta = -18^\circ$ and $\beta = +18^\circ$ (Fig. 26). According to the G-criterion instead, the crack would not branch but kink at $\beta = 0$ (simply extends). This observation may serve to show again how differently the G and HSIF-criteria may predict the fracture path, reminding that here, we are not considering the effect of the material resistance to fracturing which should be considered in the prediction of the crack path (Azhdari and Nemat-Nasser, 1996a; 1996b).

Results of peridynamic analyses of pure Mode I (MAT 4) don't show any branching, even when the MPPD S-criterion is considered, as Fig. 26 shows. This is not surprising since the HSIF-criterion and the MPPD S-criterion are theoretically different. In

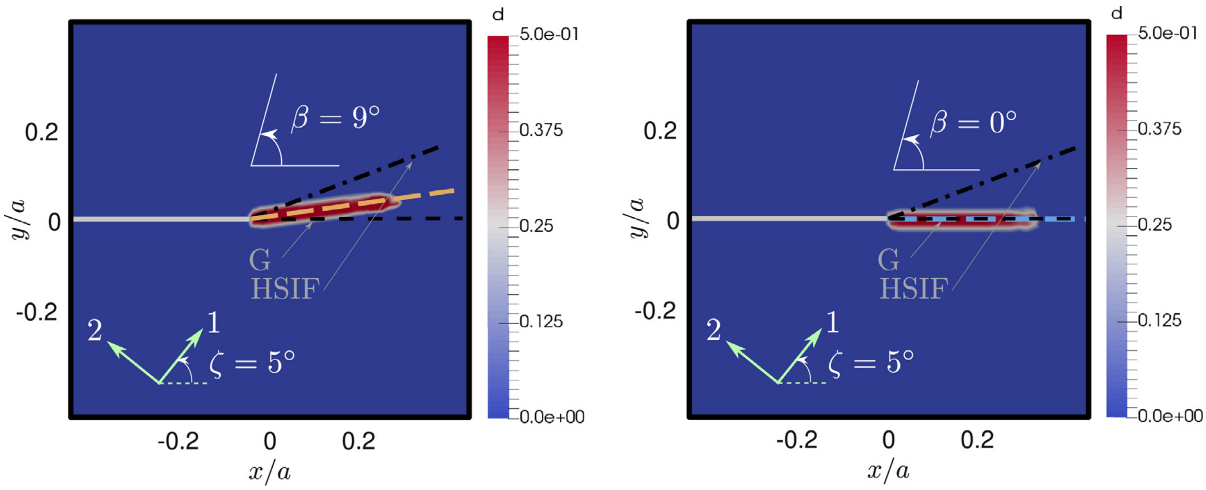

Fig. 29. MAT 4, General orthotropy, material reference system inclined at $\zeta = 5^\circ$: Crack kinking angles corresponding to a pure Mode I ($\alpha = 0^\circ$), and computed adopting the MPPD S-criterion (left) and E-criterion (right). Dashed black lines indicate the analytical predictions of the HSIF and G criteria.

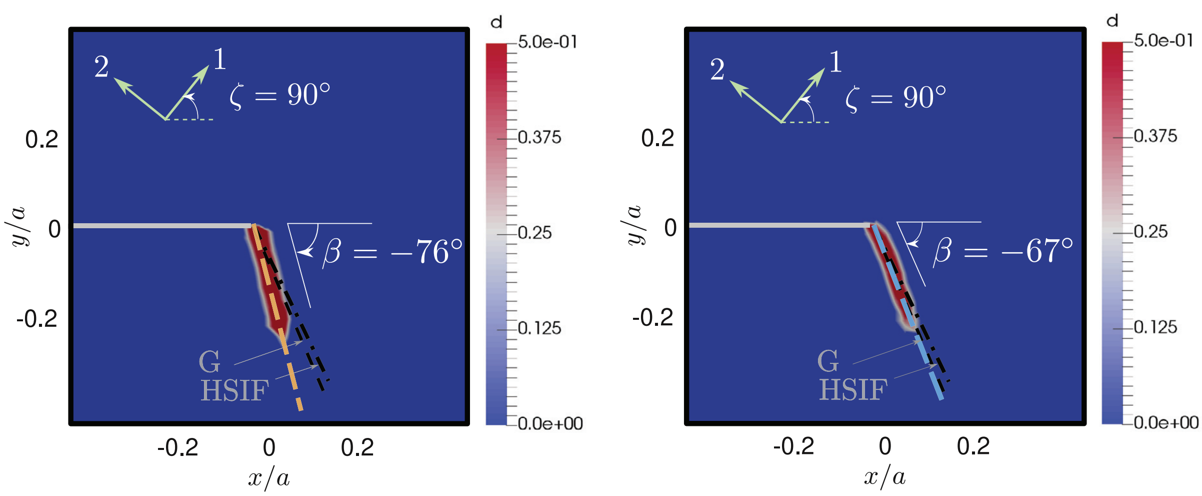

Fig. 30. MAT 4, General orthotropy, material reference system inclined at $\zeta = 90^\circ$: Crack kinking angles corresponding to a Pure Mode II ($\alpha = 90^\circ$), and computed adopting the MPPD S-criterion (left) and E-criterion (right). Dashed black lines indicate the analytical predictions of the HSIF and G criteria.

fact, the first one is a stress-based fracture criterion and the second one is a deformation-based criterion. The G-criterion and the MPPD E-criterion instead, show a conceptual similarity since they can be both considered energetic fracture criteria. However, all the classical (G and HSIF) criteria and PD failure criteria (E and S) show obvious differences from each other, and they are here compared only qualitatively, in order to show the differences in the predicted crack paths. In any case, regarding the analyses performed on general orthotropic material (MAT 4) under general mixed-Mode loading, the kinking angles predicted by the PD E-criterion seem to be fairly close to those predicted by the classical G and HSIF criteria (see Figs. 27, 28, 29 and 30). The MPPD S-criterion instead, that leads to kinking angles that are, in general, in good agreement with those corresponding to the G and HSIF classical criteria in the case of isotropy (MAT 1) or degenerate orthotropy (MAT 2), seems to suffer the lack of information about the shear component of the bond strain energy density in the other cases, at hight mode-mixity angles (Figs. 21, 22, 23, 24, 25, 26, 27, 28, 29 and 30). This evidence is more pronounced when the loading is pure shear.

In fact, under these conditions, the kinking angles computed using S-criterion and corresponding to cubic symmetry (MAT 3), and general orthotropy (MAT 4), show higher dissimilarities with respect to the angles β predicted by both the classical criteria of elasticity and the MPPD E-criterion, as shown by Figs. 21, 23, 28 and 30. This is explained by the fact that in orthotropic materials the crack front is in general locally associated with a mixed-Mode deformation, however the MPPD S-criterion does not take into account the shear deformation of the ligament. While for isotropic materials this aspect can be considered acceptable, the same may be not true in the case of anisotropic materials, in which a PD failure criterion that takes into account shearing deformations could be required for describing properly the kinking phenomenon, specially approaching pure Mode II loading conditions, where the bond shearing deformation measure should not be in general neglected.

It is worth noting at this point, that all the considerations here presented are referred exclusively to the kinking angles predicted adopting the conceived micropolar peridynamic model.

Lastly, we consider also the case of a material reference system inclined at $\zeta \neq 0$ with respect to the main crack axis x[5]. We focused the attention on MAT 4, since among the orthotropic materials considered in this study, it is the one that shows the most evident dependence of the mechanical behavior on the angle ζ. Results confirm that the kinking angles β predicted by the MPPD

[5] Some same cases discussed in Azhdari and Nemat-Nasser (1996a) are considered in this section.

failure criteria may be quite different in some cases, the same as between the classical HSIF and G fracture criteria (see Figs. 29 and 30). Another consideration is that considering a pure Mode II far-field load, while for $\zeta = 0$, the angles β computed with the MPPD criteria are smaller than those corresponding to the classical fracture criteria, in the case of $\zeta = 90^\circ$, it can be seen that there is an opposite trend (see Fig. 30): the kinking angles predicted by the E- and S-criteria are larger than the kinking angles calculated following the classical fracture criteria.

4. Conclusions

In this paper a micropolar peridynamic model is applied to the study of crack initiation and kinking in isotropic and orthotropic brittle materials under mixed mode loadings. The analytical formulation of the two-dimensional model is derived from the definition of a specific micropotential energy function for micropolar nonlocal lattices which allows for a four independent elastic constants (full orthotropic) peridynamic model that reduces to a (two independent) constants isotropic model as special case. A distinctive aspect of the conceived formulation is that the bond elastic parameters are continuous functions of the bond orientation in the principal material axes. The crack-tip problem and the kinking phenomenon is investigated by performing an analysis of the boundary layer that surrounds the front of a two dimensional crack subjected to different $K_{\rm II}^{\infty}/K_{\rm I}^{\infty}$ ratios, and assuming an isotropic surface energy. Results obtained in this study can be summarized in the following points:

- The proposed micropolar peridynamic scheme demonstrated its accuracy in predicting the displacement and the stress fields in the vicinity of a crack in orthotropic materials.
- The computed kinking angle β in isotropic materials adopting both the S-criterion and E-criterion are in good agreement with those predicted by the classical G and HSIF fracture criteria. Moreover it is shown that the Poisson's ratio of the material in MPPD can affect the computed kinking angles, especially in the case of peridynamic S-criterion and pure Mode II loading.
- The simulations of crack kinking in an orthotropic materials under general mixed-Mode loading drive home the point that the crack extension directions are sensitive to the specific criterion that is adopted. In addition, because peridynamic models rely on specific cohesive laws such as the illustrative linear one used in this paper, the angles of crack kinking they predict may differ from those predicted by a continuum theory for which the energy release rate is associated with a Dirac-Delta-type cohesive law for which only the area (energy release rate) is relevant. In fact, it is expected that if the peridynamic model presented here were to adopt a different shaped cohesive law, the crack kinking directions would change. Nevertheless it was observed that the kinking angles predicted by the peridynamic E-criterion, even adopting medium grids, are fairly close to those predicted by the classical G-criterion or HSIF criterion. With the understanding of the differences in the fundamental structure of the continuum theory and the peridynamic theory just stated, we can say a few words about the MPPD S-criterion. It leads to kinking angles that are very similar to those predicted by the E-criterion and that are, in general, in good agreement with the predictions of the G and HSIF classical criteria, in the case of isotropy or degenerate orthotropy. Computed kinking angles corresponding to general orthotropy or cubic symmetry instead, show higher dissimilarities with the angles β predicted both by the classical criteria of elasticity and the MPPD E-criterion, for deformation modes approaching pure shear. This evidence could be explained considering that in orthotropic materials the crack front is in general locally associated with a mixed-Mode deformation, and the MPPD S-criterion does not take into account the shear deformation of the ligament. While for isotropic materials this aspect can be considered acceptable, the same may be not true in the case of anisotropic materials, in which a PD failure criterion that takes into account shearing deformations could be required for describing properly the kinking phenomenon in micropolar peridynamics. However, the situation may change when considering the actual anisotropy of the fracture resistence of the material.
- The G-criterion and the conceived MPPD E-criterion show a conceptual similarity since they can be both considered energetic fracture criteria. However, it is emphasized that while the classical (G and HSIF) criteria and Peridynamic failure criteria are fundamentally different from each other, the results presented in this paper are illustrative; the 'correct' crack extension direction depends on the cohesive laws adopted and the details of the material microstructure.

The peridynamic model described in this paper provides a powerful tool for simulating crack growth in anisotropic materials and structures. However, like other computational models, it must be informed by experimental results that will shed light on what sort of crack growth criteria and what sort of cohesive laws are appropriate for a specific anisotropic material or structure.

Appendix A. Strain energy and macroelastic energy densities

Given the four deformation states described by Eqs. (40)–(43), the conventional linear elastic strain energy density functions of the orthotropic continuum are obtained by

$$\phi(\mathbf{X})_1 = \frac{1}{2}C_{ij}\epsilon_i\epsilon_j = \frac{1}{2}\begin{bmatrix} C_{11} & C_{12} & 0 \\ C_{12} & C_{22} & 0 \\ 0 & 0 & C_{66}\end{bmatrix}\begin{Bmatrix} s \\ s \\ 0\end{Bmatrix}\cdot\begin{Bmatrix} s \\ s \\ 0\end{Bmatrix}$$
$$= \frac{s^2}{2}(C_{11}+C_{22}+2C_{12}) \tag{A.1}$$

$$\phi(\mathbf{X})_2 = \frac{1}{2}C_{ij}\epsilon_i\epsilon_j = \frac{1}{2}\begin{bmatrix} C_{11} & C_{12} & 0 \\ C_{12} & C_{22} & 0 \\ 0 & 0 & C_{66}\end{bmatrix}\begin{Bmatrix} s \\ 0 \\ 0\end{Bmatrix}\cdot\begin{Bmatrix} s \\ 0 \\ 0\end{Bmatrix} = \frac{s^2}{2}C_{11} \tag{A.2}$$

$$\phi(\mathbf{X})_3 = \frac{1}{2}C_{ij}\epsilon_i\epsilon_j = \frac{1}{2}\begin{bmatrix} C_{11} & C_{12} & 0 \\ C_{12} & C_{22} & 0 \\ 0 & 0 & C_{66}\end{bmatrix}\begin{Bmatrix} 0 \\ s \\ 0\end{Bmatrix}\cdot\begin{Bmatrix} 0 \\ s \\ 0\end{Bmatrix} = \frac{s^2}{2}C_{22} \tag{A.3}$$

$$\phi(\mathbf{X})_4 = \frac{1}{2}C_{ij}\epsilon_i\epsilon_j = \frac{1}{2}\begin{bmatrix} C_{11} & C_{12} & 0 \\ C_{12} & C_{22} & 0 \\ 0 & 0 & C_{66}\end{bmatrix}\begin{Bmatrix} 0 \\ 0 \\ 2\gamma\end{Bmatrix}\cdot\begin{Bmatrix} 0 \\ 0 \\ 2\gamma\end{Bmatrix} = 2\gamma^2 C_{66} \tag{A.4}$$

The PD macroelastic energy density functions corresponding to the four deformation states described by Eqs. (40)–(43) are obtained instead substituting Eqs. (34) and (35) and Eqs. (37) and (38) in Eq. (16)

$$\Phi(\mathbf{X})_1 = \frac{1}{2}\int_{H_{\mathbf{X}}}\frac{k_n(\psi)s^2\,|\boldsymbol{\xi}|}{2}\mathrm{d}V_{\mathbf{X}'}$$
$$= \frac{1}{2}\int_0^{\delta}4\int_0^{\pi/2}\frac{k_n(\psi)ts^2\,|\boldsymbol{\xi}|^2}{2}\mathrm{d}\psi\,\mathrm{d}\xi$$
$$= \frac{t\pi s^2\delta^3}{48}(3k_{n_1}+3k_{n_2}+4k_{t_1}+2k_{\nu}) \tag{A.5}$$

$$\Phi(\mathbf{X})_2 = \frac{1}{2}\int_{H_{\mathbf{X}}}\frac{k_n(\psi)s^2(1+\cos 2\psi)^2\,|\boldsymbol{\xi}|}{8}+\frac{k_t(\psi)s^2(\sin 2\psi)^2\,|\boldsymbol{\xi}|}{8}\mathrm{d}V_{\mathbf{X}'}$$

$$= \frac{1}{2}\int_0^{\delta} 4 \int_0^{\pi/2} \frac{k_n(\psi) t s^2 (1+\cos 2\psi)^2 \, |\boldsymbol{\xi}|^2}{8} + \frac{k_t(\psi) t s^2 (\sin 2\psi)^2 \, |\boldsymbol{\xi}|^2}{8} \mathrm{d}\psi \, \mathrm{d}\xi$$

$$= \frac{t\pi s^2 \delta^3}{768}(38k_{n_1} + 6k_{n_2} + 24k_{t_1} + 4k_{\nu}) \tag{A.6}$$

$$\Phi(\mathbf{X})_3 = \frac{1}{2}\int_{H_{\mathbf{X}}} \frac{k_n(\psi) s^2 (1-\cos 2\psi)^2 \, |\boldsymbol{\xi}|}{8} + \frac{k_t(\psi) s^2 (\sin 2\psi)^2 \, |\boldsymbol{\xi}|}{8} dV_{\mathbf{X}'}$$

$$= \frac{1}{2}\int_0^{\delta} 4 \int_0^{\pi/2} \frac{k_n(\psi) t s^2 (1-\cos 2\psi)^2 \, |\boldsymbol{\xi}|^2}{8} + \frac{k_t(\psi) t s^2 (\sin 2\psi)^2 \, |\boldsymbol{\xi}|^2}{8} \mathrm{d}\psi \, \mathrm{d}\xi$$

$$= \frac{t\pi s^2 \delta^3}{768}(6k_{n_1} + 38k_{n_2} + 24k_{t_1} + 4k_{\nu}) \tag{A.7}$$

$$\Phi(\mathbf{X})_4 = \frac{1}{2}\int_{H_{\mathbf{X}}} \frac{k_n(\psi) \gamma^2 (\sin 2\psi)^2 \, |\boldsymbol{\xi}|}{2} + \frac{k_t(\psi) \gamma^2 (\cos 2\psi)^2 \, |\boldsymbol{\xi}|}{2} dV_{\mathbf{X}'}$$

$$= \frac{1}{2}\int_0^{\delta} 4 \int_0^{\pi/2} \frac{k_n(\psi) t \gamma^2 (\sin 2\psi)^2 \, |\boldsymbol{\xi}|^2}{2} + \frac{k_t(\psi) t \gamma^2 (\cos 2\psi)^2 \, |\boldsymbol{\xi}|^2}{2} \mathrm{d}\psi \, \mathrm{d}\xi$$

$$= \frac{t\pi \gamma^2 \delta^3}{192}(6k_{n_1} + 6k_{n_2} + 24k_{t_1} + 4k_{\nu}) \tag{A.8}$$

References

Askari, E., Bobaru, F., Lehoucq, R.B., Parks, M.L., Silling, S.A., Weckner, O., 2008. Peridynamics for multiscale materials modeling. J. Phys. 125 (1), 12078.
Azhdari, A., Nemat-Nasser, S., 1996. Energy-release rate and crack kinking in anisotropic brittle solids. J. Mech. Phys. Solids 44 (6), 929–951.
Azhdari, A., Nemat-Nasser, S., 1996. Hoop stress intensity factor and crack-kinking in anisotropic brittle solids. Int. J. Solids Struct. 33 (14), 2023–2037.
Ballarini, R., Diana, V., Biolzi, L., Casolo, S., 2018. Bond-based peridynamic modelling of singular and nonsingular crack-tip fields. Meccanica 53 (14), 3495–3515.
Becker, T., Cannon, R., Ritchie, R., 2001. Finite crack kinking and t-stresses in functionally graded materials. Int. J. Solids Struct. 38 (32–33), 5545–5563.
Bobaru, F., Foster, J., Geubelle, P., Silling, S., 2015. Handbook of peridynamic modeling. Advances in Applied Mathematics. CRC Press.
Bobaru, F., Ha, Y., Hu, W., 2012. Damage progression from impact in layered glass modeled with peridynamics. Centr. Eur. J. Eng. 2 (4), 551–561.
Bourdin, B., Francfort, G., Marigo, J.-J., 2000. Numerical experiments in revisited brittle fracture. J. Mech. Phys. Solids 48 (4), 797–826.
Casolo, S., 2006. Macroscopic modelling of structured materials: relationship between orthotropic Cosserat continuum and rigid elements. Int. J. Solids Struct. 43 (3–4), 475–496.
Casolo, S., 2009. Macroscale modelling of microstructure damage evolution by a rigid body and spring model. J. Mech. Mater. Struct. 4 (3), 551–570.
Casolo, S., Diana, V., 2018. Modelling laminated glass beam failure via stochastic rigid body-spring model and bond-based peridynamics. Eng. Fract. Mech. 190, 331–346.
Cauchy, A., 1850. Memoire sur les systemes isotropes de points materiels. In: Oeuvres Completes - Tome II, pp. 351–386.
Chang, K.J., 1981. On the maximum strain criteriona new approach to the angled crack problem. Eng. Fract. Mech. 14 (1), 107–124.
Chen, Z., Bobaru, F., 2015. Peridynamic modeling of pitting corrosion damage. J. Mech. Phys. Solids 78, 352–381.
Chiang, C., 1991. Kinked cracks in an anisotropic material. Eng. Fract. Mech. 39 (5), 927–930.
Colavito, K., Kilic, B., Celik, E., Madenci, E., Askari, E., Silling, S., 2007. Effects of Nanoparticles on Stiffness and Impact Strength of Composites, 4, pp. 3950–3959.
Diana, V., 2019. Discrete Physically-Based Models in Solid Mechanics. Politecnico di Milano, Milano, Italy Ph.D. Dissertation.
Diana, V., Casolo, S., 2019. A bond-based micropolar peridynamic model with shear deformability: elasticity, failure properties and initial yield domains. Int. J. Solids Struct. 160, 201–231.
Diana, V., Casolo, S., 2019. A full orthotropic micropolar peridynamic formulation for linearly elastic solids. Int. J. Mech. Sci. 160, 140–155.
Dipasquale, D., Sarego, G., Zaccariotto, M., Galvanetto, U., 2017. A discussion on failure criteria for ordinary state-based peridynamics. Eng. Fract. Mech. 186, 378–398.
Dipasquale, D., Zaccariotto, M., Galvanetto, U., 2014. Crack propagation with adaptive grid refinement in 2d peridynamics. Int. J. Fract. 190 (1), 1–22.
Diyaroglu, C., Madenci, E., Phan, N., 2019. Peridynamic homogenization of microstructures with orthotropic constituents in a finite element framework. Compos. Struct. 227, 111334.
Dontsova, E., Ballarini, R., 2017. Atomistic modeling of the fracture toughness of silicon and silicon-silicon interfaces. Int. J. Fract. 207 (1), 99–122.
Erdogan, F., Sih, G., 1963. On the crack extension in plates under plane loading and transverse shear. J. Fluids Eng. 85 (4), 519–525.
Foster, J., Silling, S., Chen, W., 2011. An energy based failure criterion for use with peridynamic states. Int. J. Multiscale Comput. Eng. 9 (6), 675–687.
Gerstle, W., 2016. Introduction to Practical Peridynamics: Computational Solid Mechanics without Stress and Strain. World Scientific Publishing Co. Pte. Ltd..
Gerstle, W., Sau, N., Sakhavand, N., 2009. On Peridynamic Computational Simulation of Concrete Structures, pp. 245–264.
Gerstle, W., Sau, N., Silling, S., 2007. Peridynamic modeling of concrete structures. Nucl. Eng. Des. 237 (12), 1250–1258.
Ghajari, M., Iannucci, L., Curtis, P., 2014. A peridynamic material model for the analysis of dynamic crack propagation in orthotropic media. Comput. Methods Appl. Mech. Eng. 276, 431–452.
Griffith, A., 1920. The phenomena of rupture and flow in solids. Philos. Trans. R. Soc. London 221, 163–198.
He, M.-Y., Hutchinson, J., 1989. Kinking of a crack out of an interface. J. Appl. Mech. 56 (2), 270–278.
Hu, W., Ha, Y., Bobaru, F., 2011. Modeling dynamic fracture and damage in a fiber-reinforced composite lamina with peridynamics. Int. J. Multiscale Comput. Eng. 9 (6), 707–726.
Hu, W., Ha, Y.D., Bobaru, F., 2012. Peridynamic model for dynamic fracture in unidirectional fiber-reinforced composites. Comput. Methods Appl. Mech. Eng. 217–220, 247–261.
Hu, Y., Madenci, E., 2016. Bond-based peridynamic modeling of composite laminates with arbitrary fiber orientation and stacking sequence. Compos. Struct. 153, 139–175.
le Hu, Y., Yu, Y., Wang, H., 2014. Peridynamic analytical method for progressive damage in notched composite laminates. Compos. Struct. 108, 801–810.
Huajian, G., Cheng-Hsin, C., 1992. Slightly curved or kinked cracks in anisotropic elastic solids. Int. J. Solids Struct. 29 (8), 947–972.
Jiang, C., Zhao, G.-F., Khalili, N., 2017. On crack propagation in brittle material using the distinct lattice spring model. Int. J. Solids Struct. 118–119, 41–57.
Karihaloo, B., Shao, P., Xiao, Q., 2003. Lattice modelling of the failure of particle composites. Eng. Fract. Mech. 70 (17), 2385–2406.
Keating, P., 1966. Effect of the invariance requirements on the elastic moduli of a sheet containing circular holes. J. Mech. Phys. Solids 40, 1031–1051.
Khan, S.M., Khraisheh, M.K., 2000. Analysis of mixed mode crack initiation angles under various loading conditions. Eng. Fract. Mech. 67 (5), 397–419.
Kilic, B., Agwai, A., Madenci, E., 2009. Peridynamic theory for progressive damage prediction in center-cracked composite laminates. Compos. Struct. 90 (2), 141–151.
Lehoucq, R., Silling, S., 2008. Force flux and the peridynamic stress tensor. J. Mech. Phys. Solids 56 (4), 1566–1577.
Lekhnitskii, S.G., 1963. Theory of Elasticity of an Anisotropic Body. Holden-Day, Inc., San Francisco, CA.
Li, Wei-Jian, Zhu, Qi-Zhi, Ni, Tao, 2020. A local strain-based implementation strategy for the extended peridynamic model with bond rotation. Computer Methods in Applied Mechanics and Engineering 358, 112625.
Lilliu, G., van Mier, J., 2003. 3D lattice type fracture model for concrete. Eng. Fract. Mech. 70 (7), 927–941.
Liu, W., Hong, J.-W., 2012. Discretized peridynamics for linear elastic solids. Comput. Mech. 50 (5), 579–590.
Madenci, E., Oterkus, E., 2014. Peridynamic Theory and its Applications.
Madenci, E., Oterkus, S., 2016. Ordinary state-based peridynamics for plastic deformation according to Von Mises yield criteria with isotropic hardening. J. Mech. Phys. Solids 86, 192–219.
Matlab, 2017. Matlab 2017 A (Programmimng Language).
Miehe, C., Welschinger, F., Hofacker, M., 2010. Thermodynamically consistent phase–field models of fracture: variational principles and multi-field fe implementations. Int. J. Numer. Methods Eng. 83 (10), 1273–1311.
Mikata, Y., 2018. Linear peridynamics for isotropic and anisotropic materials. Int. J. Solids Struct..
Navier, C.L., 1827. Memoire sur les lois de l'equilibre et du mouvement des corps solides elastique. Memoires de l'Institut 6, 375–384.
Ni, T., Zaccariotto, M., Zhu, Q.-Z., Galvanetto, U., 2019. Static solution of crack propagation problems in peridynamics. Comput. Methods Appl. Mech. Eng. 346, 126–151.
Obata, M., Nemat-Nasser, S., Goto, Y., 1989. Branched cracks in anisotropic elastic solids. J. Appl. Mech. 56 (4), 858–864.
Ostoja-Starzewski, M., 2002. Lattice models in micromechanics. Appl. Mech. Rev. 55 (1), 35–59.
Oterkus, E., Madenci, E., 2012. Peridynamic analysis of fiber-reinforced composite materials. J. Mech. Mater. Struct. 7 (1), 45–84.
Oterkus, S., Madenci, E., Agwai, A., 2014. Fully coupled peridynamic thermomechanics. J. Mech. Phys. Solids 64, 1–23.
Pan, Z., Ma, R., Wang, D., Chen, A., 2018. A review of lattice type model in fracture mechanics: theory, applications, and perspectives. Eng. Fract. Mech. 190, 382–409.

Panchadhara, R., Gordon, P.A., 2016. Application of peridynamic stress intensity factors to dynamic fracture initiation and propagation. Int. J. Fract. 201 (1), 81–96.
Paris, P.C., 2014. A brief history of the crack tip stress intensity factor and its application. Meccanica 49 (4), 759–764.
Rabczuk, T., Ren, H., 2017. A peridynamics formulation for quasi-static fracture and contact in rock. Eng. Geol. 225, 42–48.
Rahaman, M.M., Roy, P., Roy, D., Reddy, J., 2017. A peridynamic model for plasticity: micro-inertia based flow rule, entropy equivalence and localization residuals. Comput. Methods Appl. Mech. Eng. 327, 369–391.
Ren, H., Zhuang, X., Rabczuk, T., 2016. A new peridynamic formulation with shear deformation for elastic solid. J. Micromech. Mol. Phys. 1 (2), 1650009.
Roy, P., Pathrikar, A., Deepu, S., Roy, D., 2017. Peridynamics damage model through phase field theory. Int. J. Mech. Sci. 128–129, 181–193.
Saint Venant, A.B.d., 1845. Note sur la pression dans lintérieur des corps ou à leurs surfaces de séparation. Compt. Rend. Hebdomad. Séan. Acad. Sci. 1, 24–26.
Shojaei, A., Mossaiby, F., Zaccariotto, M., Galvanetto, U., 2018. An adaptive multi–grid peridynamic method for dynamic fracture analysis. Int. J. Mech. Sci. 144, 600–617.
Sih, G., Paris, P., Irwin, G., 1965. On cracks in rectilinearly anisotropic bodies. Int. J. Fract. 1 (3), 189–203.
Sih, G.C., 1974. Strain-energy-density factor applied to mixed mode crack problems. Int. J. Fract. 10 (3), 305–321.
Silling, S., 2000. Reformulation of elasticity theory for discontinuities and long-range forces. J. Mech. Phys. Solids 48 (1), 175–209.
Silling, S., Askari, E., 2005. A meshfree method based on the peridynamic model of solid mechanics. Comput. Struct. 83 (17–18), 1526–1535.
Silling, S., Epton, M., Weckner, O., Xu, J., Askari, E., 2007. Peridynamic states and constitutive modeling. J. Elast. 88 (2), 151–184.
Silling, S., Lehoucq, R., 2008. Convergence of peridynamics to classical elasticity theory. J. Elast. 93 (1), 13–37.
Stakgold, I., 1950. The cauchy relations in a molecular theory of elasticity. Q top Q. Appl. Math. 8 (2), 169–186.
Stukowski, A., 2009. Visualization and analysis of atomistic simulation data with OVITO–the open visualization tool. Modell. Simul. Mater. Sci. Eng. 18 (1), 15012.
Suo, Z., 1990. Domination specimens for orthotopic materials. J. Appl. Mech. 57 (3), 627–634.
Timoshenko, S., 1983. History of Strength of Materials. Dover, New York.
Truesdell, C., 1984. Timoshenko's History of Strength of Materials (1953). Springer New York, New York, NY, pp. 251–253.
Voigt, W., 1887. Theoretische studien ðber die elasticittsverhltnisse der krystalle. Abh. Ges. Wiss. Gottingen 34, 3–51.
Wang, Y., Zhou, X., Shou, Y., 2017. The modeling of crack propagation and coalescence in rocks under uniaxial compression using the novel conjugated bond-based peridynamics. Int. J. Mech. Sci. 128–129, 614–643.
Wang, Y., Zhou, X., Wang, Y., Shou, Y., 2018. A 3-d conjugated bond-pair-based peridynamic formulation for initiation and propagation of cracks in brittle solids. Int. J. Solids Struct. 134, 89–115.
Warren, T.L., Silling, S.A., Askari, A., Weckner, O., Epton, M.A., Xu, J., 2009. A non-ordinary state-based peridynamic method to model solid material deformation and fracture. Int. J. Solids Struct. 46 (5), 1186–1195.
Weckner, O., Mohamed, N.A.N., 2013. Viscoelastic material models in peridynamics. Appl. Math. Comput. 219 (11), 6039–6043.
Williams, J.G., Ewing, P.D., 1984. Fracture under complex stress — the angled crack problem. Int. J. Fract. 26 (4), 346–351.
Wu, C.H., 1978. Maximum-energy-release-rate criterion applied to a tension-compression specimen with crack. J. Elast. 8 (3), 235–257.
Xu, J., Askari, A., Weckner, O., Silling, S., 2008. Peridynamic analysis of impact damage in composite laminates. J Aerosp Eng 21 (3), 187–194.
Yaghoobi, A., Chorzepa, M. G., 2017. Fracture analysis of fiber reinforced concrete structures in the micropolar peridynamic analysis framework. Engineering Fracture Mechanics 169, 238–250.
Zhang, G., Gazonas, G.A., Bobaru, F., 2018. Supershear damage propagation and sub-rayleigh crack growth from edge-on impact: a peridynamic analysis. Int. J. Impact Eng. 113, 73–87.
Zhou, W., Liu, D., Liu, N., 2017. Analyzing dynamic fracture process in fiber-reinforced composite materials with a peridynamic model. Eng. Fract. Mech. 178, 60–76.
Zhu, Q., Ni, T., 2017. Peridynamic formulations enriched with bond rotation effects. Int. J. Eng. Sci. 121, 118–129.